Title:
The Shuram excursion: A response to climate extremes at the dawn of animal life

Kristin D. Bergmann[1*], Magdalena R. Osburn[2], Julia Wilcots[1], Marjorie Cantine[1,3], John P. Grotzinger[4], Woodward W. Fischer[4], John M. Eiler[4], Magali Bonifacie[5]

[1]Department of Earth, Atmospheric and Planetary Sciences, Massachusetts Institute of Technology, Cambridge, MA 02139

[2]Department of Earth and Planetary Sciences, Northwestern University Evanston, IL 60208

[3]now at Department of Geosciences, Goethe-Universität Frankfort, Germany

[4]Division of Geological and Planetary Sciences, California Institute of Technology Pasadena, CA 91125

[5]Institut de Physique du Globe de Paris, Universit$\acute{e}$ Paris Cit$\acute{e}$ 1 Rue Jussieu, 75005 Paris, France

[*]To whom correspondence should be addressed; E-mail: kdberg@mit.edu.

The Ediacaran-aged Shuram excursion was the last and largest of the Neoproterozoic negative carbon isotope anomalies. Recognized in stratigraphic successions around the globe, it precedes diverse evidence for macroscopic, multicellular life, and follows the Cryogenian global glaciations and Ediacaran Gaskiers glaciation. Hypotheses for the cause of the Shuram excursion can be broadly grouped into those that argue for post-depositional diagenetic alter-

ation of the carbon isotope record (*1–7*) and those that argue the extremely low δ^{13}C values reflect a primary perturbation to the carbon cycle (*8–10*). Given the timing and magnitude of this event, distinguishing between these disparate hypotheses, or combining them, is critical for reconstructing the environmental conditions under which complex life evolved on Earth. We test specific predictions of each model using a range of stratigraphic observations and micro- and macro-analytical techniques. We find that the type sections in Oman where the Shuram excursion was first described are well preserved and contain a range of features difficult to reconcile with a post-depositional origin. However, many salient features are consistent with an extreme warming event coupled to a carbon cycle perturbation, analogous to the Paleocene-Eocene Thermal Maximum (PETM), and increased middle Ediacaran volcanism. We propose that cooling associated with the recovery was critical for origination rates of macroscopic soft-bodied organisms.

One sentence summary: An extreme hyperthermal event, linked to Ediacaran volcanism, can reconcile a range of observations associated with the Shuram excursion.

Main Text: Neoproterozoic sedimentary successions record a series of pronounced negative carbon isotope excursions. The most extreme of which, the Ediacaran-aged Shuram carbon isotope excursion (CIE), drops from baseline $\delta^{13}C_{VPDB}$ values of +5‰ to as low as 12‰ within tens of meters of vertical stratigraphic section, and then gradually recovers to +5‰ often over several hundred meters, in multiple sections globally (*11*). The Shuram excursion has been hypothesized to result from secondary (diagenetic) processes that postdate deposition and need not have a direct connection to the surface carbon cycle (*1–7*) or from primary changes in water column dissolved inorganic carbon (DIC) (*8, 9, 12*).

Arguments for a diagenetic origin for the Shuram excursion include: the extreme magnitude of negative values in the nadir, beyond mantle input values which challenge traditional global carbon isotope budget models (*1, 13*); high Mn/Sr and Fe/Ca ratios in the excursion nadir (*3*); and the association of low δ^{13}C values with anomalously low δ^{18}O values—features often interpreted as signatures of carbonate diagenesis (*2, 3, 11*). It has been suggested that diagenesis could have produced the Shuram excursion either by flushing large volumes of ^{13}C-poor waters through carbonate rocks early or late in the burial history (fluid-buffered alteration) (*2,3,6*) or by the authigenic precipitation of cements and other secondary carbonates from pore fluids with low δ^{13}C values reflecting microbial processes associated with organic diagenesis (sediment-buffered alteration) (*1, 7, 14*). Additional models using Ca isotopes suggest selective intervals of the stratigraphy experienced sediment-buffered alteration while others experienced fluid-buffered alteration (*4, 5, 15*). Each diagenetic model makes specific predictions for the petrographic character of the rocks, including high-resolution spatial variability of isotopes and elements and carbonate clumped isotope thermometry results, which can distinguish between fluid- and sediment-buffered alteration in shallowly buried successions (*16*)(Table 1).

A primary origin for the Shuram excursion is supported by the wide paleogeographic occurrence of middle Ediacaran negative CIEs. Concurrent Re/Os ages from the CIEs in Oman and NW Canada also suggest the Shuram excursion is a primary carbon cycle perturbation with a shorter duration than previously suggested (*17*). Five locations (Oman, NW Canada, Australia, Peru, and Death Valley) have similar isotopic (C, O, Ca, Sr) and bulk elemental patterns (Mn, Sr, Mg) (*15*). When viewed as a whole, the geochemical data preserve clear trends associated with a primary depositional depth gradient. Stratigraphy in Australia preserve depleted clasts in breccias deposited soon after the excursion nadir (*18*). High resolution δ^{13}C trends preserve a transgression within an ooid grainstone of Death Valley (*19*). Five other locations also demon-

strate a clear association between the onset of the excursion and sea level rise (*15*). These locations have other sedimentological features in common including climbing wave ripples and storm deposits including edgewise conglomerates (*15, 20*).

In the Phanerozoic, there is a widely recognized relationship between climate change and many CIEs identified globally (*21–23*), in part expressed as co-variation in δ^{13}C and δ^{18}O. Coupled climate and carbon cycle perturbations like the Paleocene-Eocene thermal maximum (PETM) are recorded in a wide range of sedimentologic and isotopic datasets. During the PETM, a CO_2 or methane-driven temperature increase is recorded by multiple proxies including Mg/Ca ratios of foraminifera and carbonate clumped-isotope temperature change in marine and terrestrial environments (*24, 25*). Physical consequences of warming include the thermal expansion of seawater and subsequent sea level rise, as well as a flashy hydrologic cycle characterized by severe and frequent storms (*26, 27*). Many deep-sea cores show a characteristic red clay interval associated with the PETM event horizon in otherwise carbonate-rich strata which has been interpreted as a chemical consequence of ocean acidification and a shoaling of the carbonate compensation depth (CCD) (*28*). Shallow water environments document a smaller magnitude pH change, where both environments contribute CO_2 release to the atmosphere (*29*). Anoxia and expanded oxygen minimum zones, in part due to temperature-dependent O_2 solubility, can be tracked with a variety of proxies including biomarkers and I/Ca (*30, 31*). An initial period of rapid physical weathering in a hot and arid climate with minimal chemical breakdown is represented by sands and micaceous silts at multiple localities (*32*). A transition to a warm and wet climate led to significant chemical weathering and deposition of kaolinites (*33*) and geochemical proxy evidence for enhanced weathering (i.e. ^{187}Os/^{188}Os) (*34*). Biologic consequences from warming, anoxia, and ocean acidification include extinction in the deep sea and migration and origination in both terrestrial and marine fossil records (*35*).

If the Shuram excursion is a consequence of diagenetic alteration, climate change (*12*), or both, then the consequences should be observable in the rock record (Table 1). We evaluate predictions from each diagenetic model and the PETM using sedimentology and stratigraphy, petrography, mineralogy, a range of micro-and macro-analyses of trace element and isotopic variability, and carbonate clumped isotope thermometry. We also compile known volcanic occurrences within the age range of the Shuram excursion (*17*) to identify a potential driver for climate change. If a primary coupled climate-carbon cycle perturbation model unifies the range of observations associated with Shuram excursion-hosting strata worldwide, the magnitude of δ^{18}O change predicts this is one of the most extreme surface ocean warming events in the last 600 million years.

Results and Discussion To test predictions from post-depositional diagenetic and primary models for the Shuram excursion, two stratigraphic sections were studied from shallowly buried strata in the Huqf outcrop area (Mukhaibah Dome (MD) & Khufai Dome (KD) $<$ 2 km max burial depth) (*16, 36*). The two sites preserve a range of shallow marine depositional environments through time. These results are considered in context of a more regionally and temporally extensive study of alteration in Ediacaran and Phanerozoic carbonates across Oman (*16*).

Sedimentology and Stratigraphy To assess the macroscopic predictions of each model, detailed lithofacies and sequence stratigraphic analysis was conducted. The Shuram excursion in Oman is recorded in the strata of the Khufai, Shuram and Buah formations within the Ediacaran- to Cambrian-aged Huqf Supergroup (Fig. S1) (*37–39*). In the Huqf Outcrop area, the pre-excursion strata of the Khufai Formation transition from deep-water calcitic mudstone and wackstone lithofacies to shallow water dolomitic tepees, stromatolites, and edgewise conglomerates consistent with a peritidal and shallow subtidal depositional environment (*39*). The onset of the Shuram excursion begins with sea level rise in transgressive dolomitic ooid grain-

stone, stromatolite and mudstone lithofacies of the uppermost Khufai Formation ($\delta^{13}C_{VPDB}$ of 1 to 5.3‰)(Fig. 1, supplementary text) (*39*). The nadir of the excursion ($\delta^{13}C_{VPDB}$ of 8 to 12‰) is recorded in subtidal, cross-stratified, calcitic ooid grainstones, edgewise conglomerates, and hummocky cross-stratified, red, micaceous, siliciclastic siltstones of the Shuram Formation (*38*). The recovery of the excursion ($\delta^{13}C_{VPDB}$ values of 8 to +2‰) occurs in a thick limestone succession (∼200 m) of subtidal crinkly laminated mudstone, edgewise conglomerates and large meter-scale domal stromatolites of the Buah Formation (*40*). A type two sequence boundary occurs near the contact between the Shuram Formation and Buah Formation as evidenced by increased sand, lenticular to wavy lamination, and evaporite mineral laths. As a whole, the lithofacies in the nadir and recovery of the Shuram excursion suggest storm-dominated conditions. Evidence for rapid sedimentation during the nadir includes climbing ripples and and loading structures including ball and pillow structures from dewatering.

Petrography To evaluate evidence for sediment-buffered and fluid-buffered diagenesis in preserved carbonate microfacies, we examined petrographic thin sections from throughout the excursion. Well below the onset of the excursion, the lower Khufai Formation has coarsely crystalline fabrics, evidence of dissolution and veining in the calcitic deep water mudstones and wackstones (Fig. S2, Fig. S3). The carbonates hosting the Shuram excursion however preserve small crystal sizes of micrite and microspar in mudstones, open, uncemented pores in fenestral mudstones and ooids with optically oriented, radial crystal fabrics (*16, 39, 41*)(Fig. 2, Fig. S3, Fig. S4).

Ooids, which have distinct precipitated crystals when they form from seawater, are useful indicators of fluid- or sediment-buffered alteration processes. We utilized EBSD to quantify crystal sizes and orientations of ooid fabrics from the onset and nadir of the excursion. The dolomitic ooid grainstone that records much of the onset of the Shuram excursion ($\delta^{13}C_{VPDB}$values of 0

to 5‰) includes mudstone rip-up clasts and micritic stromatolites that nucleated on the grainstone and generated topography above the oolite. The ooids are ordered dolomite today, have a plumose texture, and are often silica-cemented or silicified, particularly in the northern Huqf outcrop area (*16,39,41*). These dolomite ooids preserve a radial fabric composed of fine crystals as seen in nano-scale synchrotron-based PIC mapping (*41*).

The calcitic ooid grainstones from the nadir of the excursion ($\delta^{13}C_{VPDB}$values of -8 to -12‰) in the Shuram Formation are trough cross-stratified, and in thin section contain alternating siliciclastic and cement-rich horizons that infill around the ooids (Fig. 2A - B). The ooids have a well preserved radial fabric and are composed of elongate crystals that do not display micritization or equant-mosaic replacement texture. Electron backscatter diffraction (EBSD) demonstrates the radial crystals within the calcite ooids are oriented with the c-axis parallel to growth direction. Pore-filling cements can inherit the orientation of the nearest ooid crystal, but in general are randomly oriented (Fig. 2C - D).

Mineralogy To better understand whether mineralogical changes characteristic of Shuram excursion bearing successions (*15, 19*) represent selective alteration of primary aragonite (*4*), or some other process, we used petrography, XRD, electron backscatter detection (EBSD), electron microprobe elemental mapping and spot analysis, and strong- and weak-acid bulk-dissolutions using inductively coupled atomic emission spectrometry. The dolomite facies of the Upper Khufai Formation including the transgressive oolite, are ordered, stoichiometric dolomite today. Both x-ray diffraction (XRD) and bulk trace metal data confirm a mineralogical change from dolomite to limestone at the boundary with the Shuram Formation. Electron microprobe spot analyses of individual calcitic ooids in the nadir of the Shuram excursion indicate low Mg and Sr concentrations, consistent with the petrographic observation of radial ooid fabrics, all indicative of primary marine calcite (Mg: mean 0.44 ± 0.01%, Sr: 124 ± 29 ppm, Fe: 1712 ±

133 ppm, Mn: 815 ± 48 ppm, ± 1 S.E.)(Table S1). The edgewise conglomerates and crinkly laminites of the Upper Shuram Formation and lower Buah Formation are higher in Sr (X ppm ± 29 ppm), consistent with observations from other locations globally (*15*), indicating this interval might have been primary aragonite prior to dissolution and calcite replacement. Despite this process, the mudstones are still micrite and microspar, thus the transformation likely occurred under sediment-buffered conditions.

Trace elements To test the hypothesis that relatively high concentrations of Fe and Mn measured from bulk dissolution of the oolitic limestones in the nadir of the excursion reflect addition of Fe^{+2} and Mn^{+2} from reduced fluids during diagenesis (*1, 3*), we used three different procedures: 1. electron microprobe (EPMA) elemental mapping and spot analysis, 2. comparisons between analyses of strong- and weak-acid bulk-dissolutions using inductively coupled atomic emission spectrometry, and 3. synchrotron x-ray absorption near-edge spectroscopy (XANES). High iron concentration in EPMA spot analyses within ooids can be attributed to ultrafine inclusions of hematite, likely detrital in origin ($<$1 μm)(Fig. 2, E). EPMA maps of both elements indicate spatial variability, not homogeneously distributed elemental enrichment (Fig. S4). Some authigenic hematite has coated detrital grains and mineralized ooids along surfaces likely representing mineralization during depositional hiatuses. These surfaces are often capped by intervals lean in detrital sediments but with significant secondary cement indicating faster ooid deposition. XANES analyses indicate that iron is present primarily as Fe(III) in hematite and mixed valence in biotite (Fig. S8). The high bulk Mn contents of the oolitic grainstones (up to 3670 ppm) exceeds those of the individual ooids (mean 815 ± 48 ppm, ± 1 S.E.) and can be attributed to manganese-rich pink cements (Mg: mean 0.37 ± 0.02%, Sr: 0 ppm, Fe: 647 ± 165 ppm, Mn: 7853 ± 587 ppm, ± 1 S.E.), which fill interstices between ooids (Fig. S9). These pink cements constitute a diagenetic fabric, and confirm that the high Mn contents of

Shuram rocks are a result of post-depositional processes. However, these pink cements pre-date a second, porosity-occluding, sparry calcite cement (Mg: mean 0.33 ± 0.02%, Sr: 141 ± 37 ppm, Fe: 912 ± 109 ppm, Mn: 1532 ± 106 ppm, ± 1 S.E.) indicating they formed during early diagenesis in the shallow sediments (Fig. 2F and Fig. S9). XANES analysis indicates that most of the manganese is divalent Mn(II) and contained in manganoan calcite (Fig. S8). Iron oxides also host smaller amounts of manganese (visible in both EDS and electron microprobe maps; Fig. 2F). Thus, Fe enrichments in Shuram carbonates can be attributed to input of detrital siliciclastic with some sea-floor iron enrichment on hiatal surfaces as precipitated hematite rims around some of the detrital grains. In contrast, Mn enrichments reflect diagenetic addition of Mn^{+2} and occur in the earliest stages of cementation, presumably during or immediately after ooid deposition. We observe additional Mn variability, preserved as Mn-rich banding within the dolomite ooids associated with the onset of the Shuram excursion at the top of the Khufai Formation (*41*).

Phase-specific isotopic heterogeneity To evaluate the predictions from authigenic diagenetic models (*1, 7, 14*) predicting isotopically light carbonates in secondary, authigenic phases within the nadir of the CIE, we used Secondary Ion Mass Spectrometry (SIMS) to analyze disparate carbonate phases formed at different times (ooids, early Mn-rich pink cements, and clear blocky porosity occluding cement). Authigenic explanations for the low δ^{13}C value of the bulk rock would predict the Mn-rich or porosity occluding blocky cements would be ^{13}C poor relative to the ooids. SIMS analysis of two samples from a similar stratigraphic horizon, but located $\sim$15 km apart, indicate that ooids have similar carbon and oxygen isotopic compositions to authigenic early manganese-rich pink cements, and porosity-occluding blocky spar cements (Fig. S9). The striking homogeneity in the SIMS measurements of ooids and cements suggests that these phases reflect primary conditions and precipitated from similar fluids and temperatures

or were consistently altered with fluid-buffered diagenesis. Within the context of the above petrographic and trace element variability of these three phases, the former is more likely.

Crystallization temperature and fluid composition To further evaluate predictions of fluid- and sediment-buffered diagenesis at various points in the stratigraphy, carbonate clumped isotope thermometry analyses were performed on a range of carbonate facies. Carbonates with different initial characteristics (e.g., porosity, permeability, and mineralogy) will experience variable fluid-sediment interaction, which can result in co-variation of the fluid/sediment reaction temperature, carbonate $\delta^{18}O_{VPDB}$, and water $\delta^{18}O_{VSMOW}$. Cross-plots of these variables will differentiate between packages of rocks that underwent fluid- or sediment-buffered alteration. If any of the intervals (including the transgressive dolomites or the low $\delta^{13}C$ calcites) of the Shuram excursion experienced fluid-buffered alteration as suggested in previous studies, a diverse suite of samples should reveal a trend of increasing reaction temperature at relatively invariant $\delta^{18}O_{VSMOW}$ of water—near 0‰ if fluids are marine or more ^{18}O-depleted water if meteoric (orange, green and blue trajectories in Fig. 3A). If, instead, lithification or alteration occurred in sediment-buffered conditions, then water $\delta^{18}O$ and temperature will increase while carbonate $\delta^{18}O$ remains constant (purple trajectory in Fig. 3A).

When plotted in this space, a correlation of temperature vs. carbonate $\delta^{18}O$ values indicative of fluid-buffered alteration is only evident in the lower Khufai Formation, deposited well prior to the onset of the Shuram excursion (Fig. 3C). Carbonates with the highest temperatures are macroscopically coarsely crystalline (Fig. S1). The data trend indicates that water $\delta^{18}O_{VSMOW}$ values remain near 0‰ for high temperature carbonates (Fig. 3C), implying seawater-hosted diagenesis in a moderate burial environment. Notably, $\delta^{13}C$ is not correlated with $\delta^{18}O$ in the lower Khufai Formation, despite a fluid-buffered diagenetic regime. In contrast, the suite of pre-, onset-, and syn- Shuram-excursion carbonates analyzed from the upper Khufai, Shuram

and lower Buah formations have data trends indicating sediment-buffered diagenesis (Fig. 3D - F). As a group, these carbonates (squares, triangles and circles in Fig. 3) show exceptional textural preservation, moderate clumped isotope temperatures (38-78°C) and precipitation from fluids with oxygen isotope compositions similar to the range observation across modern marine environments ($\delta^{18}O_{VSMOW}$ of water = 2 to +2‰)(Fig. S12). It is important to note that the measurements in Fig. 3 average the isotopic compositions of multiple carbonate phases—including primary ooids and other grains, mud and diagenetic cements (i.e. they are bulk measurements reflecting lithification). We note that mudstone, wackestone and finely laminated stromatolite samples with small crystal sizes and evidence for early lithification like tepee structures and carbonate intraclasts sit at the low-temperature end of the data trend in Fig. 3 (Table S1) (*16*). Samples with the highest clumped isotope temperatures are more heterogeneous and are petrographically richer in secondary cements and occur occasionally throughout the excursion. These end-member samples yield elevated $\delta^{18}O$ values (Fig. 3), implying evolved formation waters that did not freely circulate with seawater (i.e., approaching sediment-buffered conditions). An example of this process is the $\delta^{18}O$ enrichment in cement observed with SIMS analysis, which is from a sample with a higher clumped isotope temperature (54°C), suggesting the cement precipitated from evolved pore fluids, likely at slightly elevated temperatures during shallow burial. For comparison to the shallowly buried sections, samples from the deeply buried section in the Oman Mountains display the highest clumped isotope temperatures, from solid state reordering or anchimetamorphism (T = 88-152°C, $\delta^{18}O_{VSMOW}$ of water = 5-15‰ supplementary text), similar to results from deeply buried rocks hosting age-equivalent excursions (*42*).

Diagenetic alteration of strata hosting the Shuram excursion We consider the above results from sedimentology, petrography, mineralogy, trace element variability, isotopic heterogeneity, temperature, and fluid oxygen isotope composition in the context of predictions ex-

pected from various diagenetic models (Table 1). Models for a diagenetic origin for the Shuram excursion call on a range of post-depositional processes. Models that suggest the Shuram excursion is the result of fluid-buffered diagenesis by either meteoric (*2, 6*) or basinal fluids (*3*) predict fabric destruction, trace element homogeneity, and coarsening of crystal size (Table 1). In the Huqf region of Oman, carbonates hosting the Shuram excursion are notable for their well-preserved fabrics, fine crystal sizes, and spatially-distinct trace element distributions (Fig. 2 and Fig. S1). Multiple fluid-buffered diagenetic models also predict low meteoric or high basinal fluid $\delta^{18}O_{VSMOW}$ values to explain the large negative $\delta^{18}O$ excursion (*2, 3*). These distinct oxygen isotope compositions are inconsistent with seawater-like fluid $\delta^{18}O_{VSMOW}$ values calculated from Δ_{47}-temperature measurements of these strata (Fig. 4, Fig. S12). Models suggesting that the Shuram excursion is the result of syn-sedimentary remineralization of organic matter resulting in extremely light authigenic carbonates predict a significant difference in $\delta^{13}C$ between authigenic cements and primary carbonates (*1, 7, 14*)(Table 1). While there was a clear early authigenic phase, pink Mn-rich cements, in oolites capturing the nadir of the excursion, we found similar carbon isotope compositions of Mn-poor ooids that were in regular contact with seawater during their growth history, Mn-rich early cements and Mn-poor blocky, porosity occluding cements, using Secondary Ion Mass Spectrometry (SIMS). This isotopic homogeneity exists despite preserved elemental heterogeneity and crystallographic differences between each phase, suggesting the bulk isotopically light carbonates reflect precipitation from DIC rather than wholesale dissolution and reprecipitation(Fig. S9). Our SIMS results are consistent with those from calcitic micrites in Australia (*43*). The only phase in those rocks with a distinct carbon isotopic composition are isotopically heavy dolomite rhombs of uncertain timing (*43*). Another suite of models has suggested that all carbonate sediments of this interval began as aragonite with light Ca isotopic compositions and high Sr concentrations, using the modern Bahamian platform as an analog, and some intervals underwent selective fluid-buffered

alteration to produce heavy Ca isotopic intervals with low Sr concentrations (*4, 15, 44*)(Table 1). The above petrographic, geochemical, and isotopic observations from multiple intervals suggest that a change in primary depositional mineralogy from dolomite, to calcite, to aragonite occurred over the course of the excursion, likely affecting Sr concentrations and Ca isotopic compositions directly (see below). While diagenesis has certainly played a role in the observed rock record in Oman, we argue based on the above lines of evidence that the Shuram excursion as expressed in Oman departs from the diagenetic expectations of post-depositional Shuram excursion models (Table 1).

Evidence for a coupled climate-carbon cycle event If diagenetic alteration cannot account for our multi-proxy observations of the carbonates hosting the Shuram excursion in Oman, we instead explore our results in the context of the predictions of a coupled climate-carbon cycle model (Table 1). The rich marine and terrestrial records of the PETM delineate six predictions for a climate-carbon cycle perturbation, which have ramifications for the oceans, atmosphere, land, and biosphere. Alongside co-varying δ^{13}C and δ^{18}O isotopic records, these predictions are: [1] warming with an identifiable driver, [2] sea level rise and storms, [3] ocean acidification, [4] anoxia, [5] enhanced physical and chemical weathering, and [6] extinction and radiation.

[1] Warming with Driver: To consider whether the Shuram excursion coincides with volcanic activity capable of driving a climate event, we built an inclusive database of Neoproterozoic occurrences of intrusive and extrusive igneous rocks. We classified each unit with compositional information and age constraints. The time interval of the Shuram excursion (574.0 ± 4.7 to 567.3 ± 3.0 Ma Ma) (*17*), coincides with a peak in occurrences of volcanic rocks, specifically, carbonatite-alkaline complexes. These (CO_2-rich) volcanic rocks are particularly abundant relative to other time intervals of the Neoproterozoic (Fig. S14). Large, caldera-style carbonatite deposits can be found associated with the Central Iapetus Magmatic Province (*45*), including

the Alnö complexes in Scandinavia (*46,47*), Vesely and Pogranichnoe complexes in Russia (*48*) and Sarfartoq complex in West Greenland (*49*), and associated with the Pan-African orogeny in Africa (*50–53*) and Argentina (*54*). Carbonatite-derived zircons contribute to a significant peak at 576 Ma in detrital zircon spectra from Australia (*55*). These carbonatite deposits do not have unusually depleted δ^{13}C values (5.1 to 7.3‰) (*56*), suggesting there was not a significant change in the volcanic ^{13}C input composition at this time.

Our high resolution clumped-isotope thermometry (Δ_{47}) dataset from the Huqf area of Oman documents cooler temperatures in the pre-excursion and recovery strata and warming associated with the onset of the excursion (Fig. 4). Clumped isotope temperatures and recorded water $\delta^{18}O_{VSMOW}$ from the pre-excursion peritidal evaporitic lithofacies (T = 43°C, water $\delta^{18}O_{VSMOW}$ = 0.2‰ [reported values are the mode of the density distributions, Fig. S12]) to the onset of the excursion in the transgressive lithofacies (T = 58°C, water $\delta^{18}O_{VSMOW}$ = 1.2‰) of the upper Khufai Formation dolomites record an increase in temperature and a change to less restricted seawater-like fluid oxygen isotope compositions (Fig. 4). The subtidal calcitic ooid grainstones capturing the nadir of the excursion in the Shuram Formation maintain high temperatures (60°C, 0‰) but record a difference in δ^{18}O mineral because of the difference between calcite and dolomite equilibrium mineral-water oxygen isotope fractionation factors. For this reason, we suggest the O isotope variations across the Shuram interval are preserved from the depositional and/or earliest diagenetic environment (including the environment of dolomite formation), when samples were still in close communication with unmodified seawater. The recovery of the excursion in the upper Shuram and lower Buah formations corresponds to lower clumped isotope temperatures (T = 47°C, water $\delta^{18}O_{VSMOW}$ = 0.8‰). While we interpret the absolute temperatures of these bulk rocks as somewhat elevated from depositional temperatures because they are composed of mixtures of primary sediments and shallow burial cements, we

interpret the change in temperature across the onset of the excursion as significant because it is preserved in a range of lithofacies (both dolomites and calcites) with a range of primary porosities. Interpreted within the context of a 600-million-year Δ_{47} record from Oman (*16*), solid state reordering is likely insignificant in the Huqf region. Based on these results we propose that the largest negative δ^{13}C excursion on record was coincident with an increase in shallow marine temperatures of $\sim$10-17°C(Fig. 4). While the absolute temperatures are somewhat elevated from depositional temperatures, the similarity of SIMS δ^{18}O data of ooids and early cements would suggest the coldest clumped isotope temperatures in each time bin approach primary temperatures in this shallow coastal environment.

While we recognize that this temperature change is large, multiple aspects of the Ediacaran system may have contributed to this change. Exact amounts of CO_2 from Ediacaran volcanic provinces are unknown, but carbonatites can have more CO_2 than a basaltic eruption. We anticipate multiple aspects of the Ediacaran system may have contributed to an extreme hyperthermal event. It is unknown how much CO_2 was added from the volcanism described above. There is also evidence for methane associated with Shuram excursion strata (*14*), which, if significant, could amplify rapid climate warming. Additionally, the DIC reservoir in the Ediacaran may have been larger (*57, 58*) than in the PETM (*29*). In a higher DIC ocean in the Ediacaran, an increase in temperature due to external volcanic forcing has potential to amplify warming through increased CO2 release to the atmosphere as solubility drops (*58*).

[2] Sea level rise and storms: In Oman, facies associated with subaerial exposure, evaporation and water body restriction, such as tepees, fenestral mudstones, intraclast conglomerates and small, laterally linked, stromatolites, are capped by sedimentary facies capturing sea level rise during the onset of the excursion (Fig. 1) (*39*). In Death Valley, transgressive facies recording the onset of the excursion similarly overlie restricted facies (*19*). Sea level rise associated

with the onset of the excursion appears to be a consistent feature across many sections (*15*). In Oman, our reconstructed water $\delta^{18}O_{VSMOW}$ changes from values consistent with evaporative enrichment in the peritidal tepee-stromatolite interval of the upper Khufai Formation to values consistent with open marine, ice-free conditions of 1.2‰ during marine transgression and the onset of the excursion (Fig. 1). Sea level rise could be tied to thermal expansion of seawater from warming, melting of high latitude glaciers, or displacement from young, bouyant oceanic crust associated with the opening of the Iapetus Ocean. The facies present in the excursion nadir and recovery host storm deposits including hummocky cross-stratified silts, climbing wave ripples in deeper water environments and edgewise conglomerates across broad areas of Oman, Death Valley, NW Canada, and Australia that are stacked for hundreds of meters(Fig. 1) (*15, 20, 59*). A transition in the hydrologic cycle to more stormy conditions is consistent with warming, and is similar to what is observed during the PETM (*27, 60*).

[3] Ocean Acidification and Recovery: We document textural, chemical, and isotopic evidence for primary mineralogical transformations associated with the Shuram excursion consistent with CO_2-driven ocean acidification and recovery that likely varied in severity both regionally and with depth. A dramatic facies shift in the shallow water environments preserved in Oman is consistent with a hiatus in carbonate sedimentation caused by ocean acidification. The onset of the excursion is captured in a grainstone of radial, plumose dolomite ooids with small crystal sizes ($\delta^{13}C_{VPDB}$ = +5 to 6‰) (*41*)and micritic stromatolite bioherms (*39*). These are draped and overlain by poorly consolidated siltstones, representing a potential carbonate gap. After 10s of meters, radial to banded radial calcitic ooids intercalated with siltstones with $\delta^{13}C_{VPDB}$ values of 10 to 12‰ may represent a shift from geochemical conditions favoring dolomite precipitation (*41*) to those favoring calcite precipitation (Fig. 2). Finally, the limestones capturing the recovery of the Shuram excursion consistently record high Sr concentra-

tions and light Ca isotopic compositions, consistent with a primary aragonite mineralogy, which requires a higher saturation state (*15, 19, 61*). We interpret the mineralogical change as evidence of a pH recovery and carbonate deposition following chemical weathering, as in more recent ocean acidification events (*28, 33*). A smaller deep ocean carbonate reservoir (*58, 62*) may help explain why evidence for ocean acidification and a subsequent recovery can be found in such shallow environments.

[4] Anoxia: A temperature increase of 10-17°C in shallow coastal environments would have implications for dissolved oxygen solubility. EPMA spot analyses and X-ray Absorption Near Edge Structure (XANES) spectra show that early marine cements have elevated manganese concentrations, indicating low oxygen conditions in the shallow sediments during the excursion nadir (Fig. 2). In addition, EPMA, SEM, and XANES results suggest that reported high bulk iron concentrations, previously inferred to represent dissolution and reprecipitation in anoxic burial fluids, are better explained as artifacts of leaching procedures using strong acids which dissolve detrital hematite, a component of the silts that we relate to terrestrial weathering (Fig. S5,S7)(see below). The early manganese-rich cement phase we have identified, suggests that anoxic conditions were prevalent in the shallow sediments and perhaps transiently in the water column. Yet the lack of pyrite implies sulfate reduction was less significant than manganese and iron reduction. Expanded anoxia associated with climate perturbations may amplify the importance of diagenetic processes (e.g. authigenic carbonate precipitation) and prevalence of isotopically light carbonates (e.g. from ^{13}C-poor DIC and pore fluids from enhanced organic remineralization (*21, 22*) or from methane clathrate destabilization (*14*)).

Most sediments of the Shuram excursion are extremely organic lean, unlike modern anoxic sediments. At higher temperatures, remineralization rates outpace carbon fixation rates and net primary productivity declines (*21, 22*). Both processes may explain the paucity of organic-rich

black shales during the Shuram excursion, despite organic-rich intervals both prior to and after the Shuram excursion in deep-water Oman successions (*63*). The isotopic composition of preserved organic carbon is consistent with ocean stratification leading to a difference in shallow and deep ocean records. In Oman, shallow water inorganic δ^{13}C and $\delta^{13}C_{org}$ records are negatively correlated, whereas deep water records are positively correlated (*9, 64, 65*). Spatial heterogeneity in elemental enrichments, organic abundance, and organic δ^{13}C differences between shallow and deep-water environments in Oman are consistent with a high temperature perturbation driving density and redox stratification. If carbonate deposition was often sluggish and inhibited and the depositional area was largely limited to shallow water environments (*58, 62*), the residence time of carbon would have been long, providing a mechanism to prolong the excursion.

[5] Weathering: Grain-scale observations of the voluminous silts associated with the Shuram excursion nadir in Oman and Death Valley, including grain size and mineralogy, are consistent with wind-blown loess filling accommodation in shallow water environments (*66, 67*). A significant volume of detrital hematite is present in both locations (Fig. S5) (*67*), which we suggest is analogous to climate-driven detrital hematite enrichments within PETM deposits (*68*). Poorly weathered micas that are abundant within the siltstones associated with the nadir of the excursion (Fig. S4) are replaced by clay-rich sediments in the recovery, which we link to a switch from hot and dry conditions in the nadir of the excursion to warm and wet conditions in the recovery, again analagous to PETM deposits (*32–34, 69*). The Sr isotope record is also consistent with enhanced weathering on land, rising from 0.7080 before the excursion to 0.7088 during the excursion, some of the most radiogenic values of the last billion years (*70, 71*). The physical and geochemical observations of sediments deposited during the Shuram excursion are consistent with a concurrent land-based weathering and hydrologic cycle feedback that promoted global

cooling through silicate weathering (*72*).

[6] Extinction and Radiation: Coupled climate-carbon cycle perturbations have visible effects on the fossil record in the Phanerozoic, but extinctions are difficult to recognize in a non-skeletal, microscopic fossil record. That said, evidence for extinction and subsequent origination is concurrent with the Shuram excursion. Many ornamented, organic-walled acanthomorphic acritarch microfossils disappear from the paleontological record at the onset of the Shuram excursion (*73*). Within the nadir of the excursion, organic-walled acritarchs are simple and rare, while the recovery sees a diverse range of microfossils (*73*). Macrofossils of algae, soft-bodied Ediacaran fauna, and the first biomineralizing organisms, *Cloudina* and *Namacalathus*, also appear following the recovery (*70*), although with new age constraints (*63*), many of the fauna appear in significantly younger strata (*74*). This pattern of origination following a hyperthermal is similar to what is observed following the PETM (*35*). The appearance of Ediacaran fauna first in deep water environments in Newfoundland and NW Canada and then in shallow water environments globally, is parsimonious with an expectation that deep-water environments remained cooler during and following a temperature perturbation (*75*). The Shuram excursion may represent the best candidate documented thus far for a Precambrian mass extinction, followed by a recovery period with innovation, origination, and niche expansion. This suggests that the Shuram excursion represented a critical bottleneck and turning point for the evolutionary advances required for macroscopic, multicellular animal life.

Conclusions In summary, our climate driven model with coupled carbon cycle effects unifies a range of sedimentological, geochemical, and biological observations of the globally-distributed Shuram excursion. We contend that a range of evidence supports warming including sea level rise, increased storm intensity, ocean acidification and recovery, anoxia, a concurrent terrestrial weathering event, and extinction. By connecting observations consistent with climate

change consequences to the timing and duration results (*63*), we identify a compelling CO_2-rich volcanic driver using a compilation of late Precambrian volcanism. These observations pose challenges to our understanding of internal feedbacks in the carbon cycle and climate system in deep time. The Shuram excursion, the largest negative carbon isotope excursion in Earth History, is best understood as one of the most extreme hyperthermal events yet documented, and as such was likely both a critical bottleneck for complex life and also spurred origination of diverse soft-bodied Ediacaran fauna in its aftermath.

References and Notes

1. D. P. Schrag, J. A. Higgins, F. A. Macdonald, D. T. Johnston, Authigenic carbonate and the history of the global carbon cycle. *Science* **339**, 540–3 (2013).

2. L. P. Knauth, M. J. Kennedy, The late Precambrian greening of the Earth. *Nature* **460**, 728–732 (2009).

3. L. A. Derry, A burial diagenesis origin for the Ediacaran Shuram-Wonoka carbon isotope anomaly. *Earth Planet. Sci. Lett.* **294**, 152–162 (2010).

4. J. A. Higgins, C. L. Blättler, E. A. Lundstrom, D. P. Santiago-Ramos, A. A. Akhtar, A.-S. Crü Ger Ahm, O. Bialik, C. Holmden, H. Bradbury, S. T. Murray, P. K. Swart, Mineralogy, early marine diagenesis, and the chemistry of shallow-water carbonate sediments. *Geochim. Cosmochim. Acta* **220**, 512–534 (2018).

5. A.-S. C. Ahm, C. J. Bjerrum, C. L. Blättler, P. K. Swart, J. A. Higgins, Quantifying early marine diagenesis in shallow-water carbonate sediments. *Geochim. Cosmochim. Acta* **236**, 140–159 (2018).

6. G.-Y. Wei, J. Wang, N. J. Planavsky, M. Zhao, E. W. Bolton, L. Jiang, D. Asael, W. Wei, H.-F. Ling, On the origin of shuram carbon isotope excursion in south china and its implication for ediacaran atmospheric oxygen levels. *Precambrian Research* **375**, 106673 (2022).

7. L. Jiang, N. Planavsky, M. Zhao, W. Liu, X. Wang, Authigenic origin for a massive negative carbon isotope excursion. *Geology* **47**, 115–118 (2019).

8. D. H. Rothman, J. M. Hayes, R. E. Summons, Dynamics of the Neoproterozoic carbon cycle. *Proc. Natl. Acad. Sci. USA* **100**, 8124–8129 (2003).

9. D. a. Fike, J. P. Grotzinger, L. M. Pratt, R. E. Summons, Oxidation of the Ediacaran ocean. *Nature* **444**, 744–7 (2006).

10. C. J. Bjerrum, D. E. Canfield, Towards a quantitative understanding of the late Neoproterozoic carbon cycle. *Proc. Natl. Acad. Sci.* **108**, 5542–5547 (2011).

11. J. P. Grotzinger, D. A. Fike, W. W. Fischer, Enigmatic origin of the largest-known carbon isotope excursion in Earth's history (2011).

12. C. J. Bjerrum, D. E. Canfield, Towards a quantitative understanding of the late Neoproterozoic carbon cycle. *Proc. Natl. Acad. Sci.* **108**, 5542–5547 (2011).

13. T. F. Bristow, M. J. Kennedy, Carbon isotope excursions and the oxidant budget of the Ediacaran atmosphere and ocean. *Geology* **36**, 863–866 (2008).

14. H. Cui, A. J. Kaufman, S. Xiao, C. Zhou, X.-M. Liu, Was the Ediacaran Shuram Excursion a globally synchronized early diagenetic event? Insights from methane-derived authigenic carbonates in the uppermost Doushantuo Formation, South China (2016).

15. J. F. Busch, E. B. Hodgin, A.-S. C. Ahm, J. M. Husson, F. A. Macdonald, K. D. Bergmann, J. A. Higgins, J. V. Strauss, Global and local drivers of the ediacaran shuram carbon isotope excursion. *Earth and Planetary Science Letters* **579**, 117368 (2022).

16. K. D. Bergmann, S. A. Al Balushi, T. J. MacKey, J. P. Grotzinger, J. M. Eiler, A 600-million-year carbonate clumped-isotope record from the Sultanate of Oman. *J. Sediment. Res.* **88**, 960–979 (2018).

17. A. D. Rooney, M. D. Cantine, K. D. Bergmann, I. Gómez-Pérez, B. Al Baloushi, T. H. Boag, J. F. Busch, E. A. Sperling, J. V. Strauss, Calibrating the coevolution of Ediacaran life and environment. *Proc. Natl. Acad. Sci. U. S. A.* **117**, 16824–16830 (2020).

18. J. M. Husson, A. C. Maloof, B. Schoene, A syn-depositional age for Earth's deepest δ13C excursion required by isotope conglomerate tests. *Terra Nov.* **24**, 318–325 (2012).

19. K. Bergmann, R. Zentmyer, W. Fischer, The stratigraphic expression of a large negative carbon isotope excursion from the ediacaran johnnie formation, death valley. *Precambrian Res.* **188** (2011).

20. J. M. Husson, A. C. Maloof, B. Schoene, Stratigraphic expression of Earth's deepest δ13C excursion in the Wonoka Formation of South Australia. *Am. J. Sci.* (2015).

21. S. M. Stanley, Relation of Phanerozoic stable isotope excursions to climate, bacterial metabolism, and major extinctions. *Proc. Natl. Acad. Sci. U. S. A.* **107**, 19185–19189 (2010).

22. S. Finnegan, D. A. Fike, D. Jones, W. W. Fischer, A Temperature-Dependent Positive Feedback on the Magnitude of Carbon Isotope Excursions. *Geosci. Canada* **39** (2012).

507 23. S. K. Turner, Pliocene switch in orbital-scale carbon cycle/climate dynamics. *Paleo-*
508 *ceanography* **29**, 1256–1266 (2014).

509 24. D. Evans, N. Sagoo, W. Renema, L. J. Cotton, W. Müller, J. A. Todd, P. K. Saraswati,
510 P. Stassen, M. Ziegler, P. N. Pearson, *et al.*, Eocene greenhouse climate revealed by cou-
511 pled clumped isotope-mg/ca thermometry. *Proceedings of the National Academy of Sci-*
512 *ences* **115**, 1174–1179 (2018).

513 25. G. N. Inglis, M. J. Carmichael, A. Farnsworth, D. J. Lunt, R. D. Pancost, A long-term,
514 high-latitude record of Eocene hydrological change in the Greenland region. *Palaeogeogr.*
515 *Palaeoclimatol. Palaeoecol.* **537** (2020).

516 26. A. Sluijs, U. Röhl, S. Schouten, H. J. Brumsack, F. Sangiorgi, J. S. Sinninghe Damsté,
517 H. Brinkhuis, late Paleocene - Early Eocene paleoenvironments with special emphasis on
518 the Paleocene-Eocene thermal maximum (Lomonosov Ridge, Integrated Ocean Drilling
519 Program Expedition 302). *Paleoceanography* **23**, PA1S11 (2008).

520 27. M. J. Carmichael, R. D. Pancost, D. J. Lunt, Changes in the occurrence of extreme precip-
521 itation events at the paleocene–eocene thermal maximum. *Earth and Planetary Science*
522 *Letters* **501**, 24–36 (2018).

523 28. J. C. Zachos, U. Röhl, S. A. Schellenberg, A. Sluijs, D. A. Hodell, D. C. Kelly, E. Thomas,
524 M. Nicolo, I. Raffi, L. J. Lourens, H. McCarren, D. Kroon, Paleoclimate: Rapid acidifi-
525 cation of the ocean during the paleocene-eocene thermal maximum. *Science (80-.).* **308**,
526 1611–1615 (2005).

527 29. D. A. Harper, B. Cascales-Miñana, T. Servais, Early Palaeozoic diversifications and ex-
528 tinctions in the marine biosphere: A continuum of change. *Geol. Mag.* **157**, 5–21 (2020).

30. X. Zhou, E. Thomas, R. E. Rickaby, A. M. Winguth, Z. Lu, I/Ca evidence for upper ocean deoxygenation during the PETM. *Paleoceanography* **29**, 964–975 (2014).

31. A. Sluijs, L. Van Roij, G. Harrington, S. Schouten, J. Sessa, L. LeVay, G.-J. Reichart, C. Slomp, Warming, euxinia and sea level rise during the paleocene–eocene thermal maximum on the gulf coastal plain: implications for ocean oxygenation and nutrient cycling. *Climate of the Past* **10**, 1421–1439 (2014).

32. V. Pujalte, J. Baceta, B. Schmitz, A massive input of coarse-grained siliciclastics in the pyrenean basin during the petm: the missing ingredient in a coeval abrupt change in hydrological regime. *Climate of the Past* **11**, 1653–1672 (2015).

33. D. C. Kelly, J. C. Zachos, T. J. Bralower, S. A. Schellenberg, Enhanced terrestrial weathering/runoff and surface ocean carbonate production during the recovery stages of the paleocene-eocene thermal maximum. *Paleoceanography* **20** (2005).

34. R. Wieczorek, M. S. Fantle, L. R. Kump, G. Ravizza, Geochemical evidence for volcanic activity prior to and enhanced terrestrial weathering during the paleocene eocene thermal maximum. *Geochimica et Cosmochimica Acta* **119**, 391–410 (2013).

35. R. Speijer, C. Scheibner, P. Stassen, A.-M. M. Morsi, Response of marine ecosystems to deep-time global warming: A synthesis of biotic patterns across the paleocene-eocene thermal maximum (petm). *Austrian Journal of Earth Sciences* **105**, 6–16 (2012).

36. M. R. Osburn, J. Owens, K. D. Bergmann, T. W. Lyons, Dynamic changes in sulfate sulfur isotopes preceding the Ediacaran Shuram Excursion. *Geochim. Cosmochim. Acta* (2015).

37. S. J. Burns, A. Matter, Carbon isotopic record of the latest Proterozoic from Oman. *Eclogae Geol. Helv.* **86**, 595–607 (1993).

551 38. E. Le Guerroué, P. A. Allen, A. Cozzi, Chemostratigraphic and sedimentological frame-
552 work of the largest negative carbon isotopic excursion in earth history: The neoproterozoic
553 Shuram formation (Nafun Group, Oman). *Precambrian Res.* **146**, 68–92 (2006).

554 39. M. Osburn, J. Grotzinger, K. Bergmann, Facies, stratigraphy, and evolution of a middle
555 ediacaran carbonate ramp: Khufai formation, sultanate of Oman. *Am. Assoc. Pet. Geol.*
556 *Bull.* **98**, 1631–1667 (2014).

557 40. A. Cozzi, P. A. Allen, J. P. Grotzinger, Understanding carbonate ramp dynamics using
558 d13C profiles: Examples from the Neoproterozoic Buah Formation of Oman. *Terra Nov.*
559 **16**, 62–67 (2004).

560 41. J. Wilcots, P. Gilbert, K. Bergmann, Nanoscale crystal fabric preserved in dolomite ooids
561 at the onset of the ediacaran shuram excursion. *Geophysical Research Letters* (PrePrint).

562 42. S. J. Loyd, F. A. Corsetti, R. A. Eagle, J. W. Hagadorn, Y. Shen, X. Zhang, M. Bonifa-
563 cie, A. K. Tripati, Evolution of Neoproterozoic Wonoka-Shuram Anomaly-aged carbon-
564 ates: Evidence from clumped isotope paleothermometry. *Precambrian Res.* **264**, 179–191
565 (2015).

566 43. J. M. Husson, B. J. Linzmeier, K. Kitajima, A. Ishida, A. C. Maloof, B. Schoene, S. E.
567 Peters, J. W. Valley, Large isotopic variability at the micron-scale in 'Shuram' excursion
568 carbonates from South Australia. *Earth Planet. Sci. Lett.* **538** (2020).

569 44. A.-S. C. Ahm, C. J. Bjerrum, C. L. Blättler, P. K. Swart, J. A. Higgins, Quantifying early
570 marine diagenesis in shallow-water carbonate sediments. *Geochim. Cosmochim. Acta* **236**,
571 140–159 (2018).

572 45. N. Youbi, R. E. Ernst, U. Söderlund, M. A. Boumehdi, A. A. Lahna, C. C. G. Tassinari,
573 W. El Moume, M. K. Bensalah, The central iapetus magmatic province: An updated re-

574 view and link with the ca. 580 ma gaskiers glaciation. *Mass Extinctions, Volcanism, and*
575 *Impacts: New Developments* **544**, 35–66 (2020).

576 46. A. M. Andersson, A. Malehmir, V. R. Troll, M. Dehghannejad, M. Andersson,
577 A. Malehmir, V. R. Troll, M. Dehghannejad, C. Juhlin, M. Ask, Carbonatite ring-
578 complexes explained by caldera-style volcanism. *Sci. Rep.* **3**, 1–9 (2013).

579 47. M. Andersson, *3D Structure and Emplacement of the Alnö Alkaline and Carbonatite*
580 (2015).

581 48. A. G. Doroshkevich, G. S. Ripp, N. V. Vladykin, V. M. Savatenkov, Sources of the Late
582 Riphean carbonatite magmatism of Northern Transbaikalia: Geochemical and isotope-
583 geochemical data. *Geochemistry Int.* **49**, 1195–1207 (2011).

584 49. K. Secher, L. M. Heaman, T. F. D. Nielsen, S. M. Jensen, F. Schjøth, R. A. Creaser, Tim-
585 ing of kimberlite, carbonatite, and ultramafic lamprophyre emplacement in the alkaline
586 province located 64°-67° N in southern West Greenland. *Lithos* **112**, 400–406 (2009).

587 50. K. Attoh, F. Corfu, P. M. Nude, U-Pb zircon age of deformed carbonatite and alkaline
588 rocks in the Pan-African Dahomeyide suture zone, West Africa. *Precambrian Res.* **155**,
589 251–260 (2007).

590 51. K. Burke, L. D. Ashwal, S. J. Webb, New way to map old sutures using deformed alkaline
591 rocks and carbonatites. *Geology* **31**, 391–394 (2003).

592 52. A. B. Kampunzu, M. N. Makutu, G. Rocci, J. Kramers, F. Pineau, I. Louaradf, F. Tembo,
593 Neoproterozoic Alkaline and Carbonatite Magmatism Along the Western Rift in Central-
594 Eastern Africa: Break-up of Rodinia Supercontinent and Reconstruction of Gondwana.
595 *Gondwana Res.* **1**, 155–156 (1997).

53. J. J. Veevers, Pan-Gondwanaland post-collisional extension marked by 650-500??Ma alkaline rocks and carbonatites and related detrital zircons: A review. *Earth-Science Rev.* **83**, 1–47 (2007).

54. C. Casquet, R. J. Pankhurst, C. Galindo, C. Rapela, C. M. Fanning, E. Baldo, J. Dahlquist, J. M. G. Casado, F. Colombo, A deformed alkaline igneous rock-carbonatite complex from the Western Sierras Pampeanas, Argentina: Evidence for late Neoproterozoic opening of the Clymene Ocean? *Precambrian Res.* **165**, 205–220 (2008).

55. T. Paulsen, C. Deering, J. Sliwinski, O. Bachmann, M. Guillong, Evidence for a spike in mantle carbon outgassing during the ediacaran period. *Nature Geoscience* **10**, 930–934 (2017).

56. H. P. Taylor Jr, J. Frechen, E. T. Degens, Oxygen and carbon isotope studies of carbonatites from the laacher see district, west germany and the alnö district, sweden. *Geochimica et cosmochimica acta* **31**, 407–430 (1967).

57. T. T. Isson, N. J. Planavsky, L. Coogan, E. Stewart, J. Ague, E. Bolton, S. Zhang, N. McKenzie, L. Kump, Evolution of the global carbon cycle and climate regulation on earth. *Global Biogeochemical Cycles* **34**, e2018GB006061 (2020).

58. K. D. Bergmann, J. Wilcots, T. Pico, N. Boekelheide, N. T. Anderson, M. D. Cantine, S. L. Goldberg, B. Keller, A. B. Jost, A. Eyster, Onset of carbonate biomineralization drove global reorganization of sedimentation and subsidence patterns. *Preprint at https://doi.org/10.31223/X5Z04M* (2022).

59. E. Le Guerroué, P. A. Allen, A. Cozzi, Chemostratigraphic and sedimentological framework of the largest negative carbon isotopic excursion in earth history: The neoproterozoic Shuram formation (Nafun Group, Oman). *Precambrian Res.* **146**, 68–92 (2006).

60. B. Schmitz, V. Pujalte, Abrupt increase in seasonal extreme precipitation at the paleocene-eocene boundary. *Geology* **35**, 215–218 (2007).

61. J. M. Husson, A. C. Maloof, B. Schoene, Stratigraphic expression of Earth's deepest δ13C excursion in the Wonoka Formation of South Australia. *Am. J. Sci.* (2015).

62. A. J. Ridgwell, Carbonate Deposition, Climate Stability, and Neoproterozoic Ice Ages. *Science (80-.).* **302**, 859–862 (2003).

63. A. D. Rooney, M. D. Cantine, K. D. Bergmann, I. Gómez-Pérez, B. A. Baloushi, T. H. Boag, J. F. Busch, E. A. Sperling, J. V. Strauss, Calibrating the coevolution of Ediacaran life and environment. *Proc. Natl. Acad. Sci. U. S. A.* **117**, 16824–16830 (2020).

64. C. Lee, G. D. Love, W. W. Fischer, J. P. Grotzinger, G. P. Halverson, Marine organic matter cycling during the Ediacaran Shuram excursion. *Geology* **43**, 1103–1106 (2015).

65. C. Lee, D. A. Fike, G. D. Love, A. L. Sessions, J. P. Grotzinger, R. E. Summons, W. W. Fischer, Carbon isotopes and lipid biomarkers from organic-rich facies of the Shuram Formation, Sultanate of Oman. *Geobiology* **11**, 406–419 (2013).

66. M. D. Cantine, J. B. Setera, J. A. Vantongeren, C. Mwinde, K. D. Bergmann, Grain size and transport biases in an ediacaran detrital zircon record. *Journal of Sedimentary Research* **91**, 913–928 (2021).

67. K. Bergmann, J. Grotzinger, W. Fischer, Biological influences on seafloor carbonate precipitation. *Palaios* **28** (2013).

68. E. Dallanave, L. Tauxe, G. Muttoni, D. Rio, Silicate weathering machine at work: rock magnetic data from the late paleocene–early eocene cicogna section, italy. *Geochemistry, Geophysics, Geosystems* **11** (2010).

641 69. C. Robert, J. P. Kennett, Antarctic subtropical humid episode at the Paleocene-Eocene
642 boundary: clay-mineral evidence. *Geology* **22**, 211–214 (1994).

643 70. S. Xiao, G. M. Narbonne, C. Zhou, M. Laflamme, D. V. Grazhdankin, M. Moczydlowska-
644 Vidal, H. Cui, Towards an Ediacaran time scale: Problems, protocols, and prospects.
645 *Episodes* **39**, 540–555 (2016).

646 71. G. M. Cox, G. P. Halverson, A. Poirier, D. Le Heron, J. V. Strauss, R. Stevenson, A model
647 for Cryogenian iron formation. *Earth Planet. Sci. Lett.* **433**, 280–292 (2016).

648 72. J. C. Walker, P. B. Hays, J. F. Kasting, A negative feedback mechanism for the long-term
649 stabilization of Earth's surface temperature. *J. Geophys. Res.* **86**, 9776–9782 (1981).

650 73. K. A. McFadden, J. Huang, X. Chu, G. Jiang, A. J. Kaufman, C. Zhou, X. Yuan, S. Xiao,
651 Pulsed oxidation and biological evolution in the Ediacaran Doushantuo Formation. *Proc.*
652 *Natl. Acad. Sci.* **105**, 3197–3202 (2008).

653 74. Z. An, G. Jiang, J. Tong, L. Tian, Q. Ye, H. Song, H. Song, Stratigraphic position of
654 the Ediacaran Miaohe biota and its constrains on the age of the upper Doushantuo δ13C
655 anomaly in the Yangtze Gorges area, South China. *Precambrian Res.* **271**, 243–253
656 (2015).

657 75. T. H. Boag, R. G. Stockey, L. E. Elder, P. M. Hull, E. A. Sperling, Oxygen, temperature
658 and the deep-marine stenothermal cradle of Ediacaran evolution. *Proc. R. Soc. B Biol. Sci.*
659 **285**, 20181724 (2018).

660 76. S. M. Bernasconi, M. Daeron, K. D. Bergmann, M. Bonifacie, A. N. Meckler, C. In-
661 terCarb, A community effort to improve interlaboratory standardization of the carbonate
662 clumped isotope thermometer. *Geochemistry, Geophys. Geosystems* p. submitted (2020).

77. N. Anderson, M. Bonifacie, J. Horita, A. Jost, S. Bernasconi, K. Bergmann, Assessing the need for mineral-specific dolomite and apatite clumped isotope thermometer calibrations using carbonate standardization. *Rapid Communications in Mass Spectrometry* (in prep).

78. K. J. Dennis, H. P. Affek, B. H. Passey, D. P. Schrag, J. M. Eiler, Defining an absolute reference frame for "clumped" isotope studies of CO2. *Geochim. Cosmochim. Acta* **75**, 7117–7131 (2011).

79. N. Anderson, J. R. Kelson, S. Kele, M. Daëron, M. Bonifacie, J. Horita, T. J. Mackey, C. M. John, T. Kluge, P. Petschnig, A. Jost, K. Huntington, S. Bernasconi, K. Bergmann, A unified clumped isotope thermometer calibration (0.5–1,100 c) using carbonate-based standardization. *Geophysical Research Letters* **48**, e2020GL092069 (2021).

80. J. Rosenbaum, S. M. F. Sheppard, An isotopic study of siderites, dolomites and ankerites at high temperatures. *Geochim. Cosmochim. Acta* **50**, 1147–1150 (1986).

81. P. K. Swart, S. J. Burns, J. J. Leder, Fractionation of the stable isotopes of oxygen and carbon in carbon dioxide during the reaction of calcite with phosphoric acid as a function of temperature and technique. *Chem. Geol. Isot. Geosci. Sect.* **86**, 89–96 (1991).

82. S. T. Kim, J. R. O'Neil, Equilibrium and nonequilibrium oxygen isotope effects in synthetic carbonates. *Geochim. Cosmochim. Acta* **61**, 3461–3475 (1997).

83. A. Matthews, A. Katz, Oxygen isotope fractionation during the dolomitization of calcium carbonate. *Geochim. Cosmochim. Acta* **41**, 1431–1438 (1977).

84. M. Schmidt, S. Xeflide, R. Botz, S. Mann, Oxygen isotope fractionation during synthesis of CaMg-carbonate and implications for sedimentary dolomite formation. *Geochim. Cosmochim. Acta* **69**, 4665–4674 (2005).

685 85. C. Vasconcelos, J. A. McKenzie, R. Warthmann, Calibration of the δ18O paleothermome-
686 ter for dolomite precipitated in microbial cultures and natural environments. *Geology*
687 (2005).

688 86. E. Le Guerroué, P. A. Allen, A. Cozzi, Parasequence development in the Ediacaran Shu-
689 ram Formation (Nafun Group, Oman): High-resolution stratigraphic test for primary ori-
690 gin of negative carbon isotopic ratios. *Basin Res.* **18**, 205–219 (2006).

691 87. J. P. Grotzinger, Upward shallowing platform cycles: a response to 2.2 billion years of
692 low-amplitude, high-frequency (Milankovitch band) sea level oscillations. *Paleoceanog-*
693 *raphy* **1**, 403–416 (1986).

694 88. A. Cozzi, J. P. Grotzinger, P. A. Allen, Evolution of a terminal Neoproterozoic carbonate
695 ramp system (Buah Formation, Sultanate of Oman): Effects of basement paleotopography.
696 *Bull. Geol. Soc. Am.* **116**, 1367–1384 (2004).

697 89. A. C. Ries, R. M. Shackleton, Structures in the Huqf-Haushi Uplift, east Central Oman.
698 *Geol. Soc. London, Spec. Publ.* **49**, 653–663 (1990).

699 90. V. P. Wright, A. C. Ries, S. G. Munn, Intraplatformal basin-fill deposits from the Infra-
700 cambrian Huqf Group, east central Oman. *Geol. Soc. London, Spec. Publ.* **49**, 601–616
701 (1990).

702 91. G. E. Gorin, L. G. Racz, M. R. Walter, Late Precambrian-Cambrian sediments of Huqf
703 Group, Sultanate of Oman. *Am. Assoc. Pet. Geol. Bull.* **66**, 2609–2627 (1982).

704 92. J. Dubreuilh, J. P. Platel, J. Le Métour, J. Roger, R. Wyns, F. Béchennec, A. Berthiaux,
705 Explanatory notes to the Geological map of Khaluf, Sheet NF 40-15, scale 1: 250000,
706 *Tech. rep.*, Directorate General of minerals, Oman ministry of petroleum and minerals
707 (1992).

93. G. D. Love, E. Grosjean, C. Stalvies, D. a. Fike, J. P. Grotzinger, A. S. Bradley, A. E. Kelly, M. Bhatia, W. Meredith, C. E. Snape, S. a. Bowring, D. J. Condon, R. E. Summons, Fossil steroids record the appearance of Demospongiae during the Cryogenian period. *Nature* **457**, 718–21 (2009).

94. E. Grosjean, G. D. Love, C. Stalvies, D. A. Fike, R. E. Summons, Origin of petroleum in the Neoproterozoic–Cambrian South Oman Salt Basin. *Org. Geochem.* (2009).

95. J. D. Hemingway, G. A. Henkes, A disordered kinetic model for clumped isotope bond reordering in carbonates. *Earth and Planetary Science Letters* **566**, 116962 (2021).

96. D. A. Stolper, J. M. Eiler, The kinetics of solid-state isotope-exchange reactions for clumped isotopes: A study of inorganic calcites and apatites from natural and experimental samples. *Am. J. Sci.* **315**, 363–411 (2015).

97. G. A. Henkes, B. H. Passey, E. L. Grossman, B. J. Shenton, A. Perez-Huerta, T. E. Yancey, Temperature limits for preservation of primary calcite clumped isotope paleotemperatures. *Geochim. Cosmochim. Acta* **139**, 362–382 (2014).

98. M. K. Lloyd, J. M. Eiler, P. I. Nabelek, Clumped isotope thermometry of calcite and dolomite in a contact metamorphic environment. *Geochim. Cosmochim. Acta* **197**, 323–344 (2017).

99. M. Bonifacie, D. Calmels, J. Eiler, Clumped Isotope Thermometry of Marbles as an Indicator of the Closure Temperatures of Calcite and Dolomite with Respect to Solid-State Reordering of C–O Bonds. *Mineral. Mag.* **77**, 735 (2013).

100. W. Visser, Burial and thermal history of Proterozoic source rocks in Oman. *Precambrian Res.* **54**, 15–36 (1991).

730 101. M. G. McCarron, The sedimentology and chemostratigraphy of the Nafun Group, Huqf
731 Supergroup, Oman, Phd thesis, Oxford University (1999).

Acknowledgements: K.D.B. thanks JC Creveling, Dave Johnston, and Andy Knoll for providing comments on early drafts of this work. C. Ma, J. Hurowitz, N. Kitchen, and Y. Guan provided assistance with analytical measurements. Portions of this research were carried out at the Stanford Synchrotron Radiation Lightsource, a Directorate of SLAC National Accelerator Laboratory and an Office of Science User Facility operated for the US Department of Energy Office of Science by Stanford University. S. Webb and J. Johnson helped with the XANES measurements at SLAC and provided standard data. We thank Petroleum Development Oman employees for helpful discussions, particularly Gideon Lopes Cardozo, Sven Scholten, and Irene Gomez Perez. Funding for analytical measurements was provided by the Agouron Institute and NASA Astrobiology Institute. We thank the Ministry of Oil and Gas, Sultanate of Oman for permission to publish this manuscript. Thure Cerling, Lou Derry, and an anonymous reviewer provided helpful criticism of an earlier verison of this manuscript. **Funding:** K.D.B. acknowledges funding from the Packard Foundation and NASA Exobiology Grant 80NSSC19K0464. M.D.C. was supported by a National Defense Science and Engineering Graduate Fellowship; K.D.B. and M.R.O. were supported by National Science Foundation Graduate Research Fellowships during their PhDs; **Author Contributions:** K.D.B. and W.F. conceptualized the study. K.D.B., M.R.O., and M.C. conducted field investigations. K.D.B. wrote the original draft. K.D.B contributed formal analysis, software, and visualization. All authors reviewed and edited the manuscript; **Data and materials availability:** All data are provided in the main text or in the supplementary materials. Data, figures, and code are available at Open Science Framework (link) for reviewers and will be made publicly available on manuscript acceptance.

Supplementary Materials :

Materials and Methods

Figs. S1 - S14

References (70 - 93)

Test	Climate Model	Diagenetic Models			
	this study	*Deep Burial (Derry et al., 2010)*	*Authigenic (Schrag et al., 2013)*	*Meteoric (Knauth & Kennedy, 2008)*	*Selective (Higgins et al., 2018)*
Sediment and Stratigraphy	climate change-controlled	dissol-reprecip	carbonate nodules or concretions	dissol-reprecip	dissol-reprecip in low Sr int
Petrography	early crystal preservation	dissol-large crystals	authigenic carbonate	dissol-reprecip, leaching	dissol-reprecip in low Sr int
Mineralogy	primary from pH change	no prediction	no prediction	aragonite to calcite	sed-buff int keeps high Sr
Trace elements	distinct across phases	homogenized	distinct in authig phase	homogenized	homogenized in low Sr int
Isotopic variability	homogenous from DIC reservoir	homogenized	^{13}C distinct in authig phase	homogenized	homogenized in low Sr int
Temperature and fluid composition	pre and rec low T, onset high T, marine W; sed-buff	high burial T, enriched W; sed-buff	moderate T, marine W; sed-buff	low T, meteoric W; fluid-buff	T and W vary, fluid-buff and sed-buff ints

Table 1. Proposed models of the Shuram excursion Tests of previous (diagenetic) and proposed (climate) mechanisms for the Shuram excursion using a variety of observations. Abbreviations used: Pre and rec low T (pre-recovery and post-recovery low temperature),

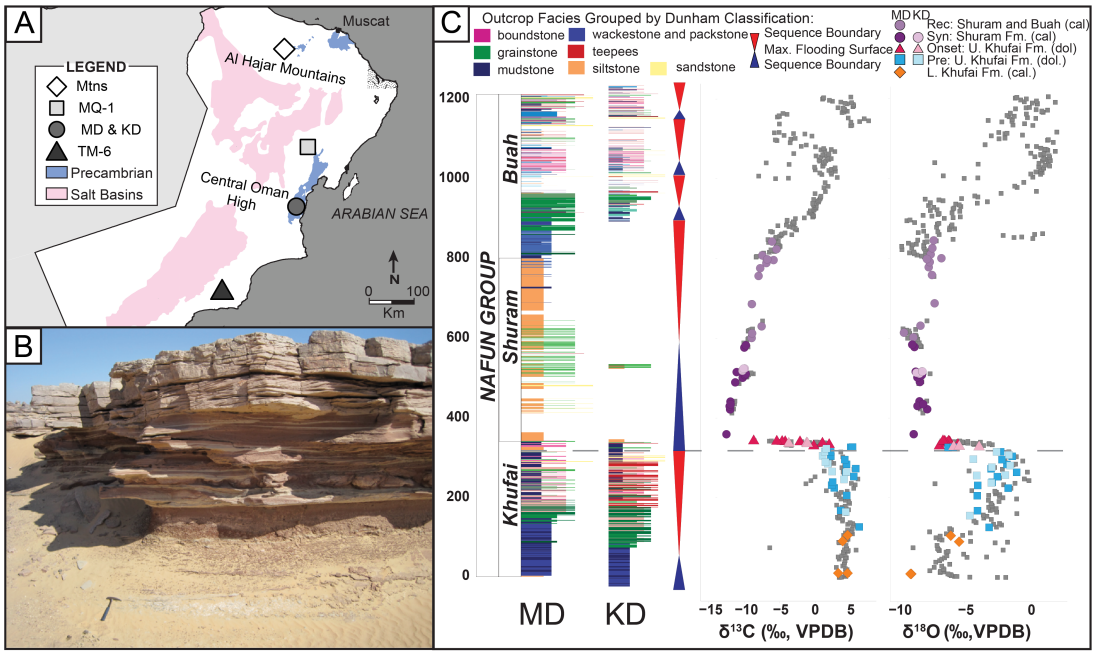

Fig. 1. The stratigraphic expression of the Shuram excursion in the Huqf region of Oman (**A**) Location map of the stratigraphic sections analyzed. (**B**) characteristic cross-stratified oolitic grainstone capping red siltstones of the Shuram Formation; hammer for scale. (**C**) Stratigraphic sections with lithofacies, $\delta^{13}C_{VPDB}$ and $\delta^{18}O_{VPDB}$ for Mukhaibah Dome (MD, dark colors) and Khufai Dome (KD, light colors) sections. The sections are aligned using the sequence boundary near the top of the Khufai Formation. Colored symbols are Δ_{47} analyses. Circles and diamonds are calcite. Squares and triangles are dolomite. Stratigraphy and grey data ($\delta^{13}C_{VPDB}$ and $\delta^{18}O_{VPDB}$) are from this study (Shuram and Buah fms.) and (Khufai Fm., (37))

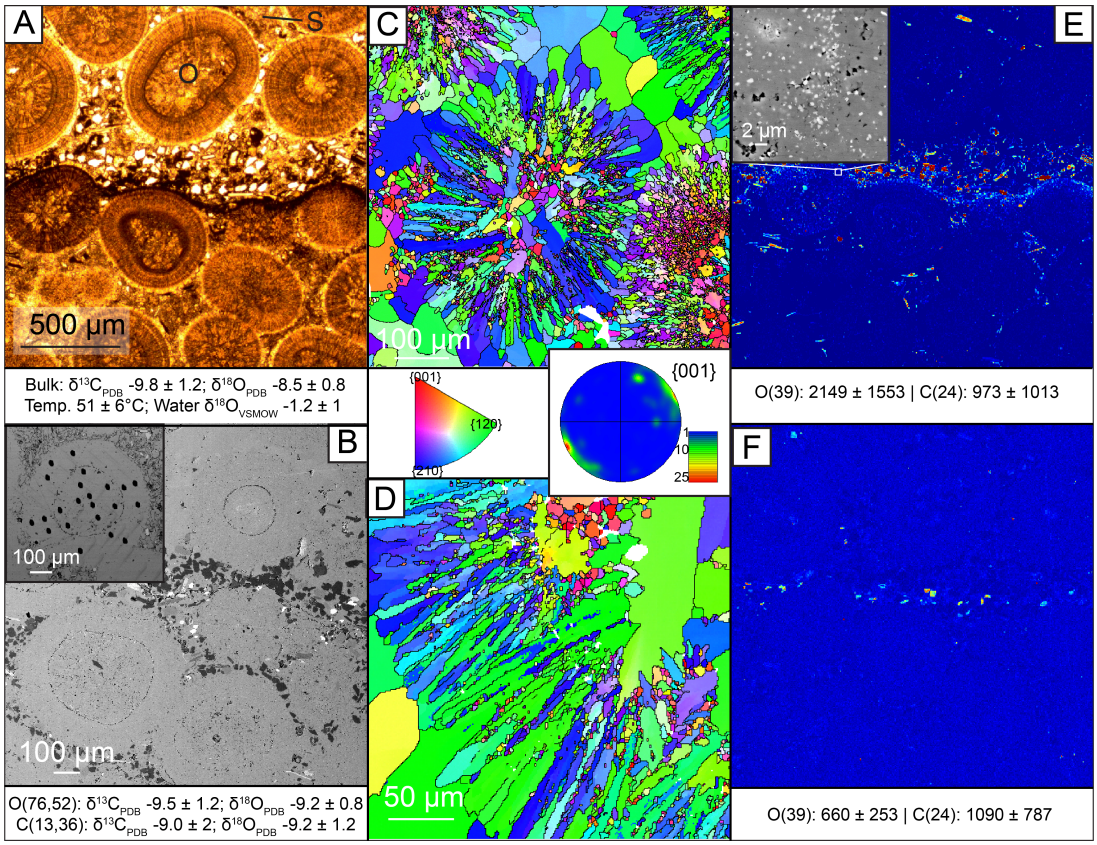

Fig. 2. Petrographic character of calcite ooids from the nadir of the excursion (**A**) Thin-section photomicrograph of ooids (o) and sediment grains (s). Bulk isotopic and clumped isotopic analyses reported below the image with 1 SE. (**B**) SEM images highlighting ooids with abundant accessory minerals infilling around the grains. The inset shows SIMS spot analyses across an ooid. SIMS measurements of ooids (o) and cement (c) are reported below the image with 1 SE. (**C,D**) electron backscatter diffraction (EBSD) crystal orientation maps and pole Figures of ooids, show primary grain orientations for this radial fabric. (**E**) Electron microprobe elemental maps of iron. The high intensities mark iron- and iron titanium oxides and biotite grains. Spot analyses of Fe concentrations (ppm) in carbonate are reported below the image with 1 SE. The inset shows finely disseminated iron oxides within the ooids. (**F**) Electron microprobe elemental maps of manganese. The high intensity domains highlight manganese

784 incorporated into oxides. Spot analyses of Mn concentrations (ppm) in carbonate are reported
785 below the image with 1 SE.

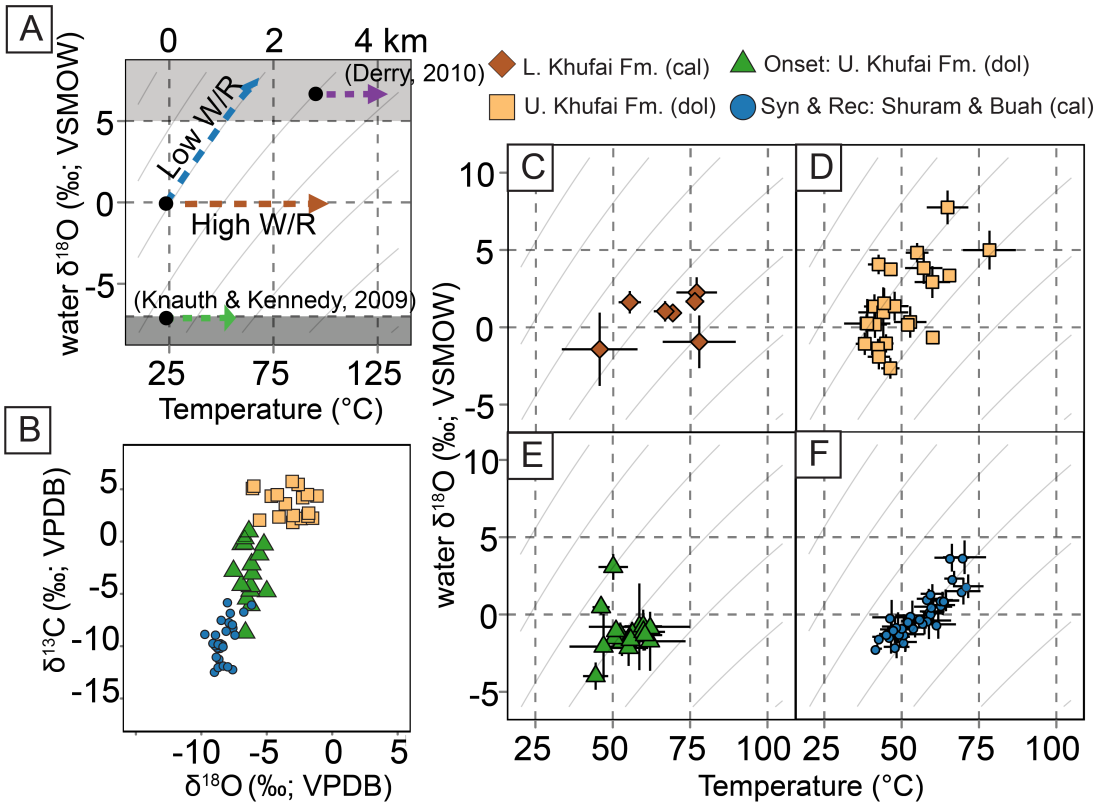

Fig. 3. Cross plots of temperature vs. fluid oxygen isotope composition. (**A**) Clumped isotope temperature vs. calculated water $\delta^{18}O_{VSMOW}$ with isopleths of carbonate $\delta^{18}O_{VPDB}$. Schematic trajectories of diagenetic processes are shown. (**B**) Cross plot of carbonate $\delta^{18}O$ and $\delta^{13}C$. (**C**) Pre-excursion samples from the lower Khufai Formation indicating fluid-buffered diagenesis. (**D**) Pre-excursions samples from the Upper Khufai Formation from a restricted peritidal environment indicating sediment-buffered diagenesis. (**E**) Uppermost Khufai Formation samples recording the onset of the excursion and sediment-buffered diagenesis. (**F**) Shuram and Buah formation samples recording the nadir and recovery of the excursion in limestone indicating sediment-buffered diagenesis.

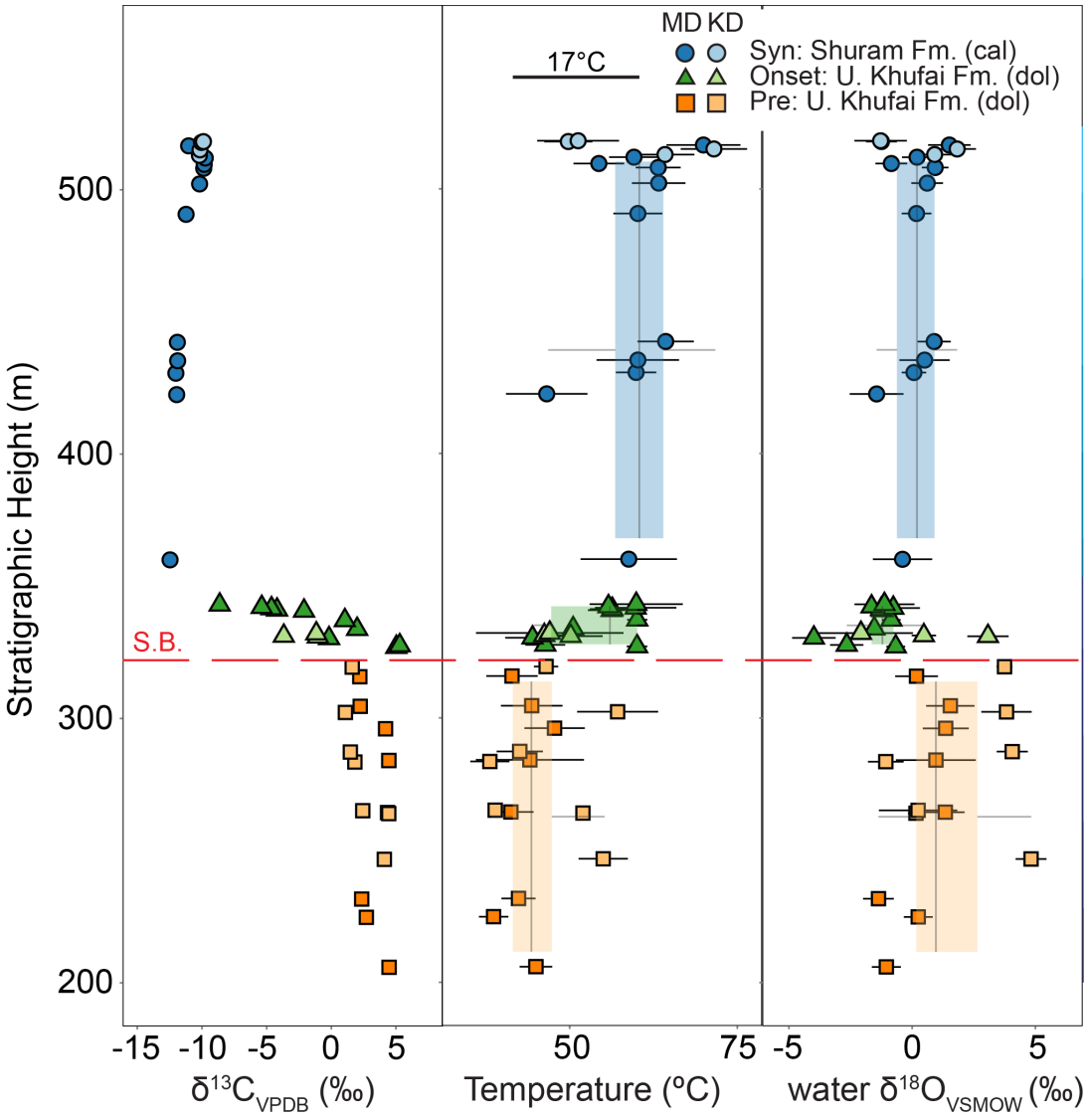

Fig. 4. Temperature and fluid oxygen isotope composition across the onset and nadir of the Shuram excursion. (**A**) Detailed stratigraphic section of the onset of the $\delta^{13}C_{VPDB}$ excursion with corresponding temperature and water $\delta^{18}O_{VSMOW}$ for MD and KD sections. Boxplots showing the minimum, maximum, standard deviation and mean for each population – pre-excursion, onset, and syn-excursion are also shown. The temperature change estimate from the modes of the density distributions of pre-excursion to syn-excursion populations are listed. Circles are calcite.

Supplementary Materials for: The Shuram excursion: A response to climate extremes at the dawn of animal life

Authors:

Kristin D. Bergmann, Magdalena Osburn, Julia Wilcots,

Marjorie Cantine, John P. Grotzinger, Woodward W. Fischer,

John M. Eiler, Magali Bonifacie

1 Materials and Methods

Sample collection and preparation Carbonate samples were collected from outcrop locations from the Huqf Outcrop area in the winters of 2010 and 2011. Stratigraphic sections were measured and sampled in stratigraphic height at Mukhaibah Dome (MD), Khufai Dome (KD) in the Huqf Outcrop area. Hand samples were cut to expose an unweathered face prior to further sampling or analysis. A variety of lithofacies were analyzed from each stratigraphic section including mudstone, stromatolite boundstone, oolitic grainstone, siltstone, sandstone and edgewise conglomerate and features like tepees(4). The textural range sampled was in part driven by necessity because no single facies persists through the entire excursion at high resolution. The added benefit of analyzing a range of carbonate facies is an improved understanding of preservation biases associated with specific carbonate textures and different primary porosities that lead to varying contributions from secondary cements. All carbonate samples analyzed in this study were composed of $> 70\%$ primary carbonate grains or micrite and $< 30\%$ post depositional diagenetic cements (estimated visually in hand sample and thin section) except when secondary veins were specifically targeted for analysis.

Bulk powder x-ray diffraction (XRD) XRD measurements were made on each powder used for clumped isotope measurements on a PANalytical X'Pert Pro within the Material Science

at the California Institute of Technology. Scans were run from 5–70° 2θ with a step size of 0.008 and a scan step time of 10.16 s. A Cu anode was used at 45 kV and 40 mA. A zero-background silicon plate was used for all measurements because of our small sample sizes. Mineralogical phases were initially identified using the X'Pert Highscore IDMin function in Jade. To determine relative abundances of calcite and dolomite in each sample, the relative peak height intensities of the major calcite and dolomite peaks at 29.5° 2θ and 30.7° 2θ, respectively, were used(23). Mixtures of known compositions of 100%, 80%, 60%, 40%, 20% and 0% calcite with dolomite were used to create the following relationship of peak height to % dolomite for the PANalytical X'Pert Pro setup at Caltech:

$$\%Dolomite = \frac{\frac{R.I.CaMg(CO_3)_2}{R.I.CaMg(CO_3)_2+CaCO_3} - 0.0526}{0.0099}$$

90% of the samples analyzed were pure end-members of either calcite or dolomite. For the 10% of samples that were a mixture of both calcite and dolomite, the acid digestion fractionation for δ^{18}O and min-water fractionation factor for all mixtures in the clumped isotope calculations were made assuming 100% composition of the dominant mineralogy. This will introduce a systematic bias for values reported from those samples, but very few samples have subequal (<70:30) carbonate mineral abundances.

SEM/electron microprobe A ZEISS 1550 VP Field Emission Scanning Electron Microscope (SEM) equipped with an Oxford INCA Energy 300 x-ray Energy Dispersive Spectrometer (EDS) system within the California Institute of Technology Geological and Planetary Sciences Division Analytical Facility was used for high-resolution imaging of each sample. Images were collected at a working distance between 7-9 mm using a Quadrant Back Scattering Detector (QBSD). In addition EDS spectroscopy measurements of individual minerals were made to identify the types of detrital minerals present in a given sample. Electron Backscatter Diffraction (EBSD) analyses were performed using Oxford AZtecHKL acquisition software on sam-

ples with 2.5-5 μm carbon coats. Kikuchi bands were collected using 20kV accelerating voltage at 70° tilt with step sizes between 0.4 and 1 μm. Data were analyzed using Oxford HKL Channel 5 software to map grain boundaries and preferred orientation. Quantitative elemental spot analysis and elemental mapping on the various carbonate components to assess trace metal variability between textures was conducted on the JEOL JXA-8200 Electron Microprobe. For all quantitative results, the accelerating voltage was 15 kV, the beam current was 20 nA, and the beam size was 1 μm. The CITZAF method was used for matrix correction. Sample standards for the five chemical elements analyzed, included: calcite for Ca, dolomite for Mg, siderite for Fe, rhodochrosite for Mn, strontianite for Sr, and anhydrite for S. Ca had an average detection limit of 177 ppm, Mg–283 ppm, Fe–323 ppm, Mn–300 ppm, Sr–589 ppm, and S–104 ppm.

Bulk powder inductively coupled plasma optical emission spectroscopy (ICP-OES) Bulk ICP measurements were completed at Actlabs and at the Jet Propulsion Laboratory (JPL) on splits of the same drilled powder. The Actlabs method digested up to 0.5 g of sample with aqua regia (HCl + NO3) for 2 hours at 95°C. Partial reactions are possible for some silicates with this dissolution method. Samples were then analyzed using a Varian ICP-OES for 35 elements. To target only the bulk limestone between 10 and 80 mg of material was digested in 10% acetic acid for 24 hours at 25°Cat the California Institute of Technology. Samples were then filtered to remove particulate oxides and diluted with HCl to minimize introduction issues with the Ar plasma source. Samples were analyzed at the Jet Propulsion Laboratory using a Thermo iCAP 6300 radial view ICP-OES with a Cetac ASX 260 autosampler with solutions aspirated to the Ar plasma using a peristaltic pump. Three standard solutions of 0.5 ppm. 5 ppm and 50 ppm of Mn, Al, Ca, K, Mg, S, Fe and Na, and three standard solutions of 0.1 ppm, 1 ppm and 10 ppm Sr in an acetic-HCl solution to matrix match were run between every 8 sample unknowns.

Bulk powder x-ray absorption near edge spectroscopy X-ray absorption near-edge spectroscopy (XANES) was conducted at the Stanford Synchrotron Radiation Lightsource (SSRL) on beam line 4-1 on five representative bulk powdered samples from the Shuram Formation in Central Oman. Samples were collected using a 3 mm rotary drill bit and further powdered using a mortar and pestle. The powdered samples were spread in a monolayer over Scotch tape and then covered with a second layer of Scotch tape. Approximately 8–16 Scotch tape layers were used for each sample, to maximize both absorbance and transmission. We used a silicon 220 Φ= 90 crystal and x-ray absorption spectra (XAS) were collected on a Ge multi-element detector for fluorescence and on an absorption detector for transmission spectra. A collimating mirror was used to reduce beam harmonics. XANES spectra of both Fe and Mn spectra were generated for each sample with a scan from 6310–7502 eV. Samples were then normalized for each element and compared to XANES spectra of known standards analyzed under similar conditions.

Secondary ion mass spectrometry (SIMS) In situ analysis of $\delta^{13}C_{VPDB}$ and $\delta^{18}O_{VPDB}$ was conducted using SIMS analysis on a Cameca 7f-GEO in the Center for Microanalysis at the California Institute of Technology. The Cameca 7f-GEO was run at a mass resolving power for C of 3000 and for O of 1800. Two thick sections of samples from the nadir of the excursion from the Mukhaibah Dome (MD) and Khufai Dome (KD) sections were embedded with in-house carbonate standards prior to polishing (Fig. S9). A 10 kV Cs^+ beam was held at 0.4 nA for C analyses and 1.1 nA for O analyses for spot sizes of 30 µm and 40 µm, respectively. Each spot was pre-sputtered for 120 s. Oxygen was measured on a two Faraday cups for a count time of 0.96 s for ^{16}O and 4.96 s for ^{18}O using a fast mass peak switching system. Carbon was measured on a single EM with a count time of 0.96 s for ^{12}C and 10.0 s for ^{13}C. Secondary ions were collected at 9 kV. 10 measurements of sample unknowns were bracketed with 4 standard analyses. Standard deviation was better than 1‰ for $\delta^{13}C$ and $\delta^{18}O$ for each of the 8 standard

analyses bracketing sets of unknowns.

Carbonate clumped isotope thermometry Samples were analyzed over the period of Jan, 2009-Jan, 2013. Samples were either micro-drilled from a thin-section billet or from a cut slab with a 3 mm rotary drill bit. 9–12 mg of powder was weighed into silver capsules before being reacted at 90°Cin 100% H_3PO_4 in a common acid bath. Evolved CO_2 was purified by multiple cryogenic traps including a Porapak-Q chromatograph held at 20°Cbefore being measured on a ThermoFinnigan MAT 253 IRMS. Methods for the measurement and corrections to analyzed heated gases run during each session following (*16*). After corrections based on the heated gas line from a given session and an intercept shift based on the initial calibration experiment, Δ_{47} values were transformed into the I-CDES reference frame (*76*) using standards measured at both MIT and Caltech (*77*). The secondary transfer function for each week was calculated using any of the following available data: 25°Cand 1000°CCO2 as well as any carbonate standards with known I-CDES values. Values within the absolute reference frame (I-CDES) for two internal standards used over the course of the analyses, Yale CM (n=35) and TV01 (n=50) were calculated from 7 weeks when 1000°CCO2 was analyzed daily and 25°CCO_2 gases were analyzed bi-weekly. The calculated values for the two standards in the absolute reference frame are reported with 1 SD for all sessions with heated gases and equilibrated gases: Yale CM Δ_{47}-I-CDES = 0.404 ± 0.022‰ (1σ, n = 33), TV01 Δ_{47}-I-CDES = 0.730 ± 0.018‰ (1σ, n = 50). Absolute reference frame values for two other internal standards run during the analytical period were calculated from weeks where either Yale CM and/or TV01 had been run with them (102-GC-AZ-01 and Carmel Chalk). Values are reported with 1 SD for all sessions with heated gases and known standards: 102-GC-AZ01 Δ_{47}-I-CDES = 0.709 ± 0.023‰ (1σ, n = 12), and Carmel Chalk Δ_{47}-I-CDES = 0.678 ± 0.020‰ (1σ, n=15). The values of the Carrara standard and 102-GC-AZ01 in the absolute reference frame are indistinguishable from those

found at Johns Hopkins (UU Carrara Δ_{47}-I-CDES = 0.403 ± 0.015‰ (1σ, n = 93) and 102-GC-AZ01 Δ_{47}-I-CDES = 0.710 ± 0.015‰ (1σ, n = 102) at Caltech (*78*). The reproducibility of standards for all analytical weeks are reported with 1 SD for all sessions: Yale CM (n = 98) Δ_{47}-I-CDES = 0.405 ± 0.019‰ 102-GC-AZ01 (n = 23) Δ_{47}-I-CDES 0.710 ± 0.011‰ TV01 (n = 86) Δ_{47}-I-CDES 0.730 ± 0.015‰ and Carmel Chalk (n = 17) Δ_{47}-I-CDES 0.675 ± 0.015‰. For single unknown measurements the uncertainty of the measurement is reported as the standard error of the mean (SEM) of Δ_{47} measurements over 8 acquisitions. For n $\geq$ 2, the error is reported as the SEM of Δ_{47} over the number of sample replicates. Temperatures were calculated in I-CDES reference frame using a calibration equation generated with available data tied to the I-CDES reference frame (*79*). The mineralogy of each powder analyzed was determined by XRD analysis (see below) to properly calculate the carbonate δ^{18}O values using unique 90°Cacid digestion fractionation factors for calcite and dolomite (*80, 81*). Fluid oxygen isotope compositions were calculated using the measured clumped isotope temperatures and separate equilibrium fractionation equations for calcite-water (*82*) and for dolomite-water (*83*). For samples that contained mixtures of calcite and dolomite, the dominant mineralogy was used to calculate carbonate δ^{18}O and water $\delta^{18}O_{VSMOW}$. Three different dolomite-water equilibrium fractionation equations were compared (*83–85*). In the main text, we present the temperature and water $\delta^{18}O_{VSMOW}$ values as the mode of a Gaussian kernel density estimate for each of the different populations (pre, onset, nadir, recovery) because some populations (i.e. nadir) have distributions that are right-skewed from sediment-buffered alteration.

Carbonate carbon and oxygen isotopic analysis In addition to the clumped isotope measurements described above, the majority of the higher resolution δ^{13}C and δ^{18}O data was analyzed at the California Institute of Technology on a ThermoFinnigan Delta V Plus attached to a ThermoFinnigan GasBench II. For the samples analyzed at Caltech, approximately 300 µg of

carbonate were weighed into gas vials, flushed with UHP He for 5 minutes and reacted with 100% H_3PO_4 at 78°Cfor 1 hour within the ThermoFinnigan GasBench II. Three standards were run at the beginning of an 88 sample run and then 8 unknown samples were bracketed by 1 standard. Standard reproducibility was better than 0.2‰ in δ^{13}C and better than 0.35‰ and 0.5‰ for δ^{18}O for two in-house standards. Additional samples were analyzed at the University of California, Riverside and University of Nevada, Las Vegas using a similar ThermoFinnigan GasBench setup. Samples analyzed at the University of Michigan weighing a minimum of 10 µg were placed in stainless steel boats. Samples were roasted at 200°Cin vacuo for one hour to remove volatile contaminants and water. Samples were then placed in individual borosilicate reaction vessels and reacted at 77° ± 1°Cwith 4 drops of anhydrous phosphoric acid for 8 minutes for calcite (12 minutes for dolomites) in a ThermoFinnigan MAT Kiel IV preparation device coupled directly to the inlet of a ThermoFinnigan MAT 253 triple collector IRMS. ^{17}O corrected data are corrected for acid fractionation and source mixing by calibration to a best-fit regression line defined by two NBS standards, NBS18 and NBS19. Data are reported in delta notation relative to VPDB. Precision and accuracy of data are monitored through daily analysis of a variety of powdered carbonate standards. At least four standards are reacted and analyzed daily. Measured precision is maintained at better than 0.1‰ for both carbon and oxygen isotope compositions.

2 Supplementary information

Geologic Setting In central Oman, the Khufai Formation is composed of shallow-water carbonates deposited on a carbonate ramp. The carbonates in the Huqf show a generalized upward shallowing of the lithofacies and lateral progradation. The lower Khufai Formation is composed of medium to thick intraclast wackestone event beds deposited below storm weather wave base (*39*). In contrast, the middle and upper Khufai Formation was deposited in a peritidal

environment with minimal accommodation space, and restriction and evaporation. These rocks display petrographic evidence for an early, fabric-retentive, dolomite formation process (*39,41*). Lithofacies include cross-bedded oncolite grainstone, tufted laminite, domal stromatolites, intraclast conglomerate and structures including teepees associated with evaporite mineral pseudomorphs and brecciation (Fig. S2) (*39*). The most proximal facies in the Upper Khufai Formation (i.e., teepees and breccia) are overlain by aggradding stromatolites and oolitic grainstone marking a sequence boundary exists where the depositional environment changes from one dominated by exposure to one characterized by slow flooding and increased accommodation space (*39*). The carbonate strata above the sequence boundary preserve the initial decline in δ^{13}C and δ^{18}O values of the Shuram excursion. The dolomitic lithofacies of the uppermost Khufai, including stromatolites and cross-stratified ooid grainstone record $\delta^{13}C_{VPDB}$ values as low as -8.5‰ (Fig. S1). One would predict this transition from a restricted evaporative environment to a flooded platform in closer connection with open marine water would be accompanied by an isotopic change in the fluid oxygen isotope composition. The maximal transgression and flooding is coincident with the introduction of massive, poorly bedded red siltstone deposits and a general loss of carbonate lithofacies marking the start of the siliciclastic dominated Shuram Formation (Fig. S2) (*38, 39*). The middle and upper Shuram Formation is better exposed in outcrop and consists of repeated parasequences of hummocky cross-stratified siltstone capped by trough to planar cross-stratified limestone ooid grainstone with $\delta^{13}C_{VPDB}$ values as low as -12‰ (Fig. S2) (*38, 86*). The siltstone contains abundant evidence for soft sediment deformation including ball and pillow structures (*86*). The recovery of the Shuram excursion occurs in the lower Buah Formation, which is also composed of shallow-water carbonates that indicate a general upward shallowing of the lithofacies. The lowermost Buah is composed of limestone crinkly laminite and edgewise conglomerate, a lithofacies interpreted as a partially lithified seafloor that is reworked and stacked on edge by oscillatory wave action (Fig. S2) (*87*). This

reworking of the seafloor likely occurred during storm events. The gradual isotopic recovery continues above a sequence boundary that shows a rapid increase in accommodation space, a shutoff in the siliciclastic input and the aggradation of large reefal stromatolite mounds filled in with trough cross-stratified grainstone shoals (Fig. S2).

In the Oman Mountains the Khufai Formation is thinner, completely limestone and is predominantly intraclast wackestone and mudstone deposited as turbidites below storm weather wave base. The Upper Khufai Formation is marked by successive large-scale (3 m) slump beds and in a few locations including Wadi Bani Awf significant coarse grained sandstone beds (*38, 39*). The Shuram Formation is dominantly composed of siltstones alternating with ripple-stratified silty carbonate grainstone beds with gutter casts on bed bottoms. The ripples indicate significant aggradation during ripple formation producing asymmetrical climbing wave ripple morphologies (Fig. S2) (*38*). The Buah Formation has a broadly similar lithofacies progression to the Huqf outcrop area with more significant lithofacies differences between Wadi Hajir and Wadi Bani Awf, the latter being more distal (*40, 88*).

Considerations for interpreting the Δ_{47} results Here we discuss potential effects of burial history, diffusive solid state reordering, and mixing on the interpretation of the clumped isotope signal across the Shuram excursion. Relevant discussion can also be found in (*16*). Maximum burial depth of the Huqf-Haushi Outcrop Area can be estimated a variety of ways. The Huqf-Haushi Outcrop Area is interpreted as an area dominated by long term uplift surrounded by the down faulted Masirah Trough and the subsiding Ghaba Salt Basin (*89, 90*). The Huqf Supergroup in the Huqf-Haushi Outcrop Area has large-scale folds trending WSW-ENE to NNE-SSW (*89*). These folds result in the Khufai Formation preserved in outcrop as a series of steeply dipping (45° or less) anticlines surrounded by shallowing dipping Shuram and Buah Formation synclines. The gently dipping to flat lying Ordovician Mahatta Humaid Formation and Upper

Carboniferous/Lower Permian Haushi Group onlap the outcrops of the Huqf Supergroup. Both the Ordovician and late Paleozoic deposits display no structural folding suggesting the deformation and uplift occurred during or shortly after deposition of the Huqf Supergroup (*89, 91*). Clay mineralogies within the Shuram and Buah Formations include illite, illite-smectite complexes, smectite and kaolinite (*92*) which suggests the Huqf-Huashi Outcrop Area hasn't experienced the full smectite-to-illite transition (burial $<$3000 m). Based on the structural history of the Huqf-Haushi Outcrop Area, we interpret the KD and MD sections as the shallowest buried of all samples analyzed for clumped isotope thermometry from Oman (*16*). As a whole the organic material from the Neoproterozoic Huqf Supergroup across Southern and Central Oman preserves a range of molecular biomarkers and sits in the marginal to middle oil window, representing some of the least thermally altered sediments of this time interval (*93, 94*).

The importance of diffusive solid state reordering on the clumped isotope thermometer has been estimated using laboratory heating experiments and reaction models (*95–97*). Estimates for optical calcite and brachiopod calcite indicate 1% reordering would occur between 115-127°C if the sample were held at those temperatures for 10 Ma and 101-112°C for 100 Ma. To achieve 99% reordered calcite in 10 Ma the modeled temperature range is 163-174°C or 144-155°C in 100 Ma (*97*). Evidence from blocking temperatures derived from marbles indicates dolomite will be much less susceptible to solid state reordering (*95, 98*). Dolomite marbles yield blocking temperatures of $\sim$300°C whereas calcite marbles yield temperatures ranging from 150-200°C (*95, 99*). If a stratigraphic section reached temperatures able to drive diffusive reordering in calcite but not dolomite, we expect the calcitic samples to yield consistently higher temperatures and calculated ^{18}O-rich compositions for the fluid. Instead, calcitic samples from the recovery in the upper Shuram Formation yield similar temperatures to the pre-excursion upper Khufai Formation. Samples from the uppermost dolomites of the Khufai Formation yield similar temperatures and fluid oxygen isotope compositions to calcites from

the lower and middle Shuram Formation. The combined estimates for minimal burial history from organic preservation and mineralogical similarities between calcite and dolomite suggest diffusive solid state reordering is not a significant process in these rocks (*16*).

Apatite thermochronology has similar to lower temperature sensitivities as calcite clumped isotope solid state re-ordering does for 100 Ma timescales and provides another point of comparison for maximum burial temperatures. Fission track ages from Huqf Supergroup detrital apatites, sourced from the 650-750 Ma granitic basement, range from 600 - 400 Ma with a peak at 450 Ma in wells from eastern Oman (*100*). This data suggests some wells never reached the apatite closure temperature of $\sim$100°C during burial and other wells experienced significant uplift around 450 Ma and saw maximum temperatures $<$100°Cfor the remainder of the Phanerozoic. Samples buried more deeply in the western part of Oman give more recent fission track ages indicating partial annealing (*100*). While high resolution analyses of the isotopic composition of end-member carbonate phases was not conducted on every sample, the SIMS analyses of ooids, clear blocky cements and early manganese-rich cements from the nadir of the excursion indicate no statistically significant differences in bulk carbon and oxygen isotopic composition between the different phases. These results indicate end-member mixing is not a significant process affecting Δ_{47} results for those samples and given the similarity in clumped isotope results between those oolitic grainstones and other samples analyzed, we infer the Δ_{47} signals are not controlled by mixing of carbonate end-members with significant isotopic differences.

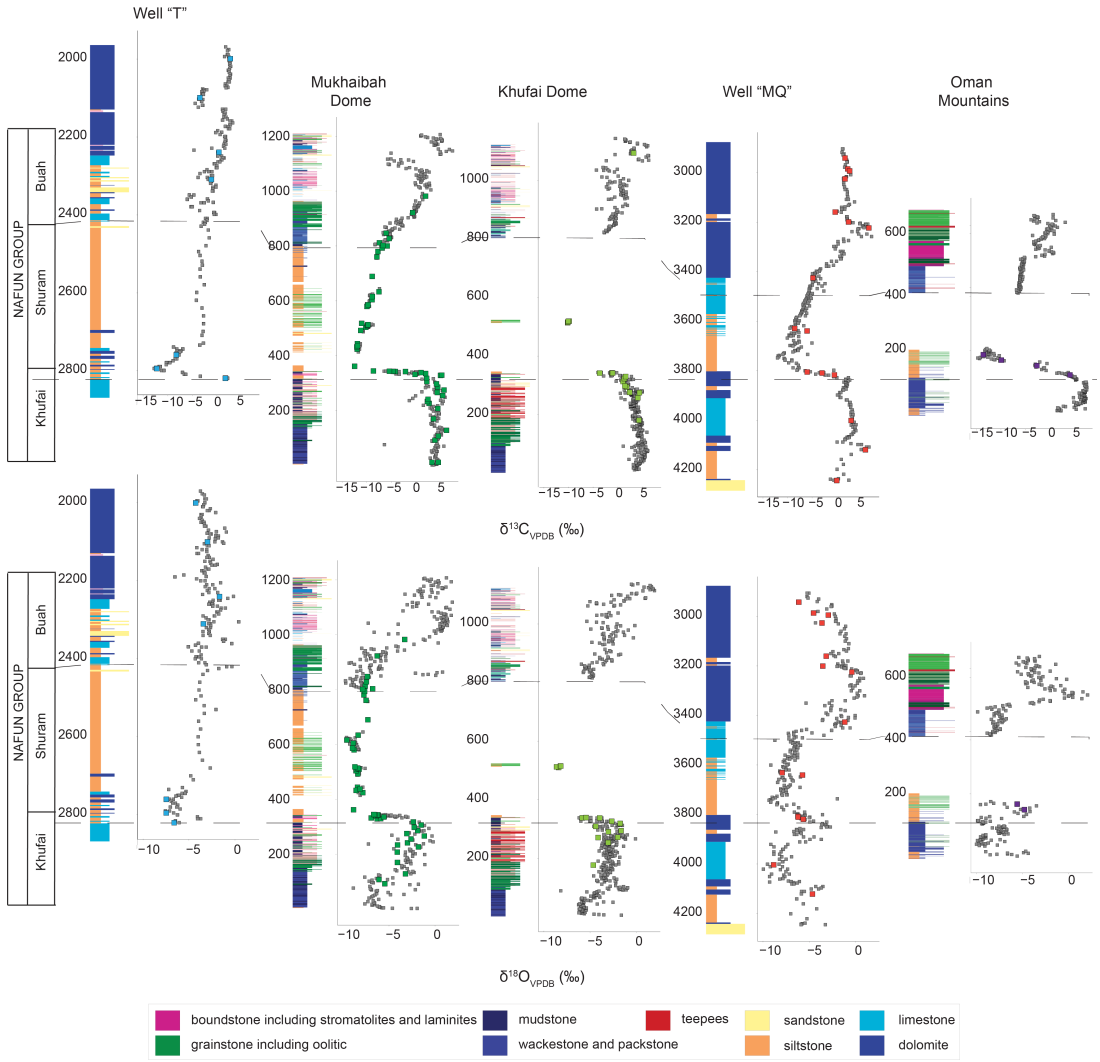

Fig. S1. Stratigraphic expression of the Shuram excursion across Oman. (**a**) δ^{13}C, δ^{18}O, and lithofacies of the five sections analyzed. Wells 'TM6' and 'MQ1' are plotted versus their current burial depth whereas 'MD' 'KD' and 'MTN' are plotted versus stratigraphic height. The sections are aligned on the onset of the Shuram excursion, which corresponds to a sequence boundary in the outcrop sections 'MD' and 'KD'. Grey data and outcrop stratigraphy from this study (Shuram and Buah fms.) and (Khufai Fm., (*36*)) and grey data for MQ1 and TM6 (*9*).

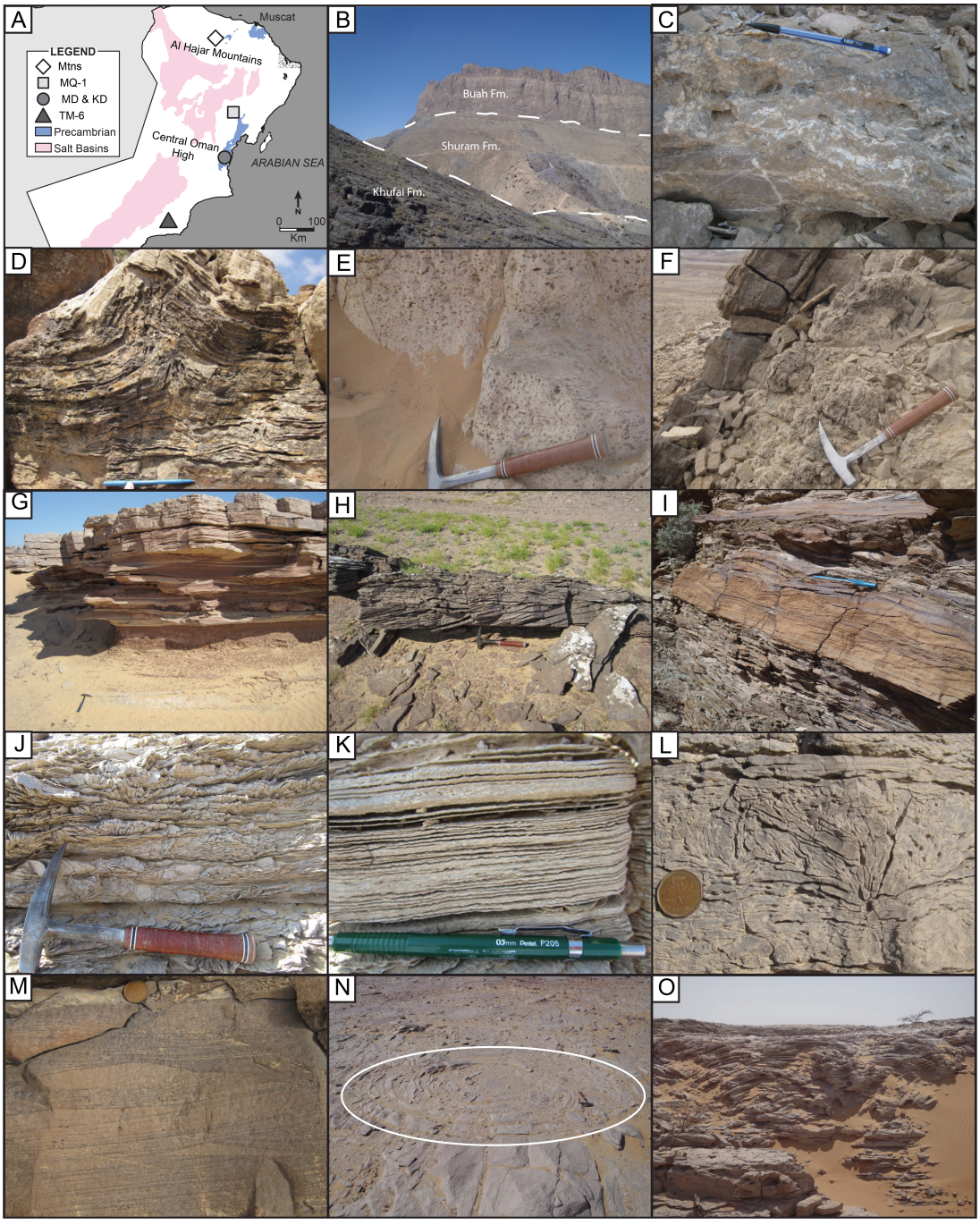

Fig. S2. Geologic context of the Shuram excursion. (**a**) Location map of the five stratigraphic sections analyzed. (**b**) Mountainside views of the three formations capturing the excursion in the Oman Mountains. (**c**) Diagenetic calcite from the Lower Khufai Formation. (**d, e**) Periti-

dal tepee and fenestral mudstone from the Upper Khufai Formation. (**f**) Transgressive systems tract recording the onset of the negative excursion in the Upper Khufai Formation. (**g, h**) Hummocky cross-stratified siltstones capped by ooid grainstones in the middle Shuram Formation. (**i**) Climbing ripples in the Shuram Formation from the Oman Mountains. (**j, k, l**), Edgewise conglomerate and crinkly laminite from the lower Buah Formation. (**m, n, o**) intraclast conglomerate and stromatolites bioherms from the Buah Formation.

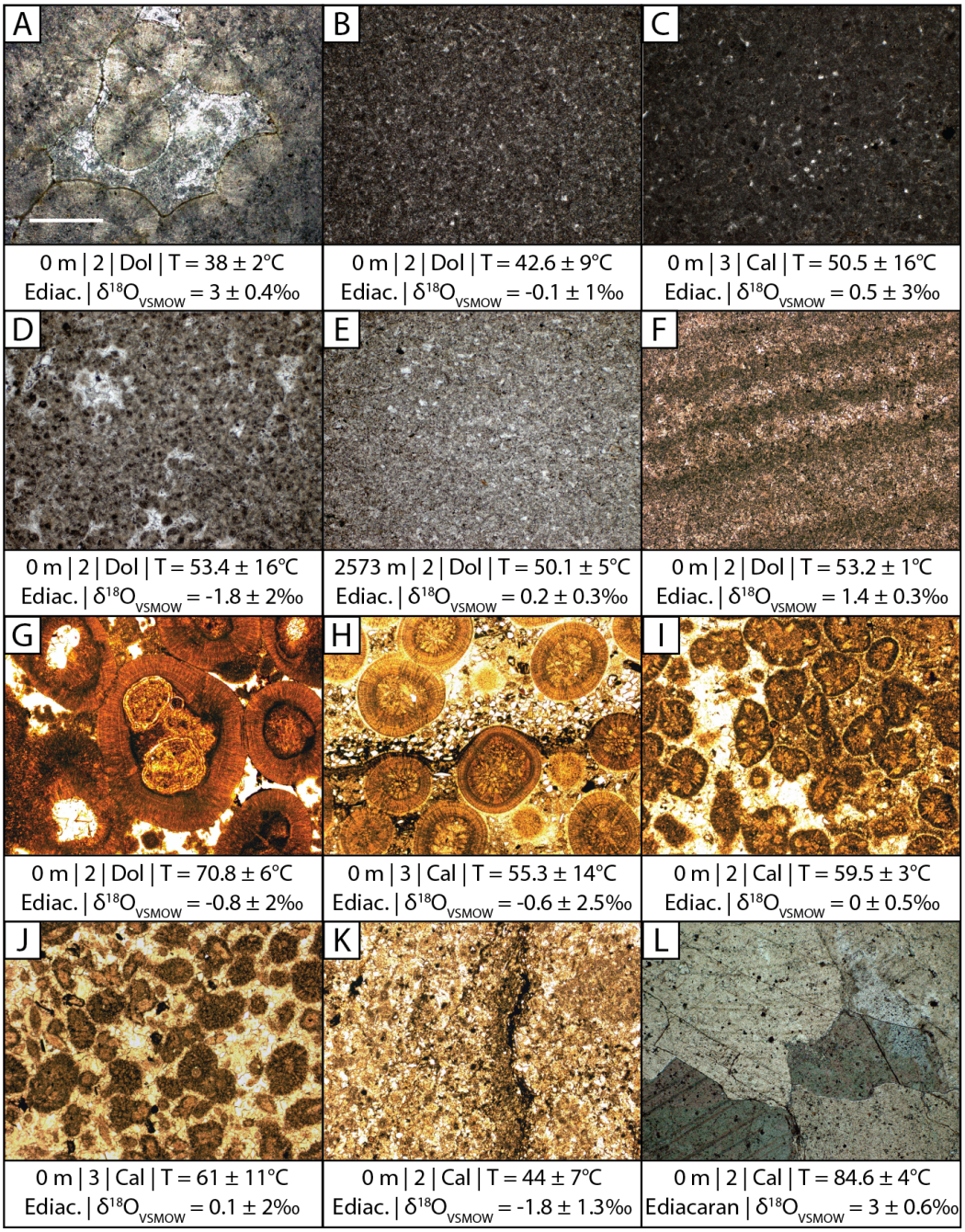

Fig. S3. Petrographic context of the Shuram excursion. Petrographic images, current burial depth, number of sample replicates, mineralogy (Dol or Cal), clumped isotope temperature and calculated water $\delta^{18}O_{VSMOW}$ for Ediacaran-aged Nafun Group carbonates. Clumped isotope and water error is ±2SE. The samples show significantly better preservation than Ara Group

carbonates (with the exception of (**l**) from one of the few intervals in the stratigraphy with macroscopic recrystallization of calcite). Epoxy is not stained blue. Scale bar in (**a**) is 500 μm and applies to all petrographic images. (**a**) Location map of the five stratigraphic sections analyzed. (**b**) Mountainside views of the three formations capturing the excursion in the Oman Mountains. (**c**) Diagenetic calcite from the Lower Khufai Formation. (**d, e**) Peritidal tepee and fenestral mudstone from the Upper Khufai Formation. (**f**) Transgressive systems tract recording the onset of the negative excursion in the Upper Khufai Formation. (**g, h**) Hummocky cross-stratified siltstones capped by ooid grainstones in the middle Shuram Formation. (**i**) Climbing ripples in the Shuram Formation from the Oman Mountains. (**j, k, l**) Edgewise conglomerate and crinkly laminite from the lower Buah Formation. (**m, n, o**) intraclast conglomerate and stromatolites bioherms from the Buah Formation.

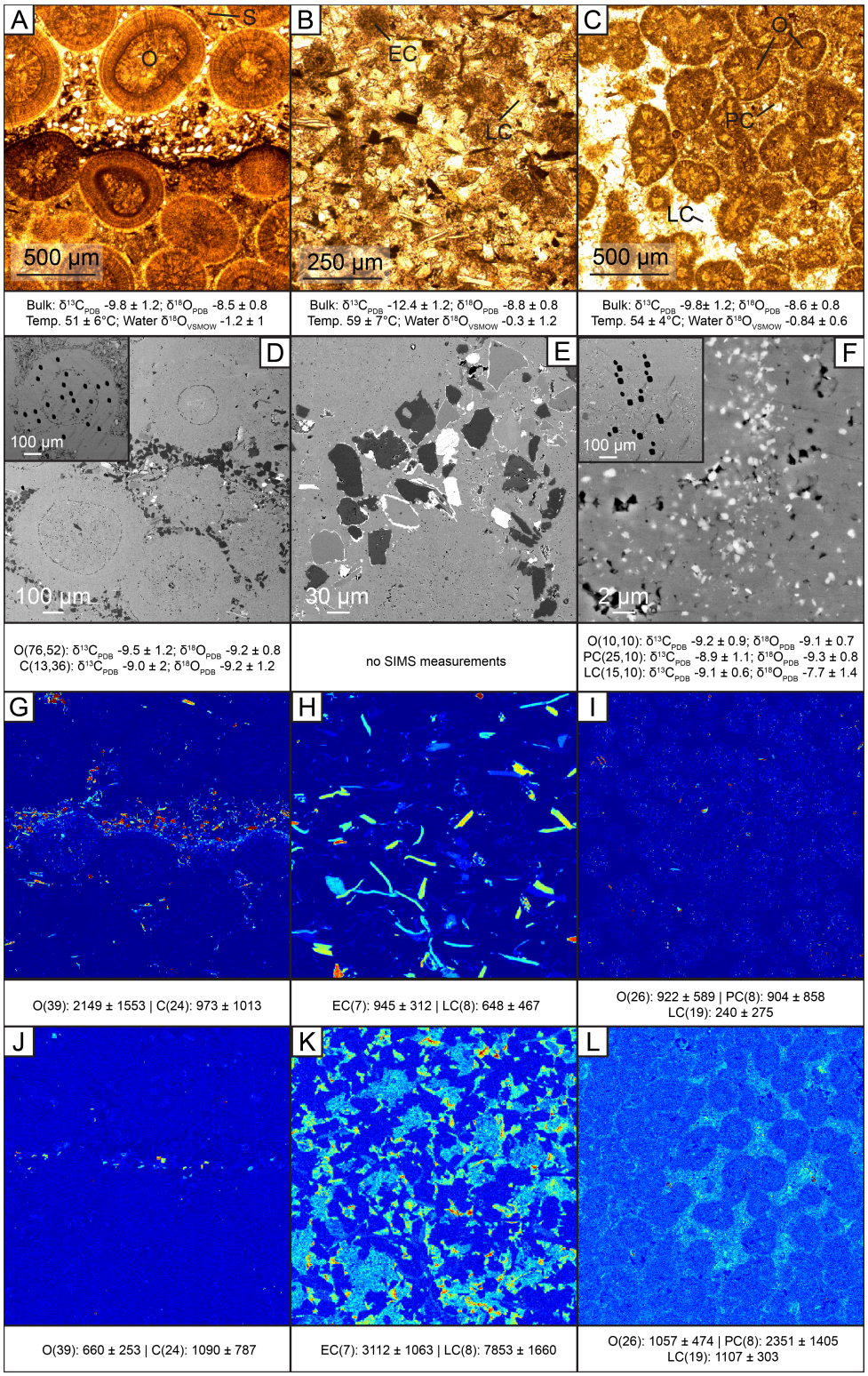
A
S
O
500 µm
B
EC
LC
250 µm
C
O
PC
LC
500 µm
Bulk: δ13CPDB -9.8 ± 1.2; δ18OPDB -8.5 ± 0.8
Temp. 51 ± 6°C; Water δ18OVSMOW -1.2 ± 1
Bulk: δ13CPDB -12.4 ± 1.2; δ18OPDB -8.8 ± 0.8
Temp. 59 ± 7°C; Water δ18OVSMOW -0.3 ± 1.2
Bulk: δ13CPDB -9.8± 1.2; δ18OPDB -8.6 ± 0.8
Temp. 54 ± 4°C; Water δ18OVSMOW -0.84 ± 0.6
D
100 µm
100 µm
E
30 µm
F
100 µm
2 µm
O(76,52): δ13CPDB -9.5 ± 1.2; δ18OPDB -9.2 ± 0.8
C(13,36): δ13CPDB -9.0 ± 2; δ18OPDB -9.2 ± 1.2
no SIMS measurements
O(10,10): δ13CPDB -9.2 ± 0.9; δ18OPDB -9.1 ± 0.7
PC(25,10): δ13CPDB -8.9 ± 1.1; δ18OPDB -9.3 ± 0.8
LC(15,10): δ13CPDB -9.1 ± 0.6; δ18OPDB -7.7 ± 1.4
G
H
I
O(39): 2149 ± 1553 | C(24): 973 ± 1013
EC(7): 945 ± 312 | LC(8): 648 ± 467
O(26): 922 ± 589 | PC(8): 904 ± 858
LC(19): 240 ± 275
J
K
L
O(39): 660 ± 253 | C(24): 1090 ± 787
EC(7): 3112 ± 1063 | LC(8): 7853 ± 1660
O(26): 1057 ± 474 | PC(8): 2351 ± 1405
LC(19): 1107 ± 303

1096

Fig. S4. In situ isotopic (SIMS) and trace metal (electron microprobe) variations. (**a, b, c**) Thin-section photomicrographs of three representative fabrics from ooid grainstones that capture the nadir of the excursion with ooids (O), sediment (S), early and late cements (EC and LC), pink cements (PC). (**d, e, f**) SEM images highlighting ooids with abundant accessory minerals infilling around the grains and within the ooids. The insets show SIMS spot analyses across ooids. SIMS measurements of ooids and cement are reported below the image with 1 SD. (**h, i, j**) Electron microprobe elemental maps of iron in the three samples shown in a-c. The high intensities in h are dominantly iron oxides whereas in i they are dominantly biotite grains. Spot analyses of Fe concentrations in carbonate are reported below each image with 1 SD. (**k, l, m**) Electron microprobe elemental maps of manganese. The high intensity areas in k are due to manganese incorporated into oxides whereas in l and m the high intensity areas are in authigenic carbonate cements. Spot analyses of Mn concentrations in carbonate are reported below each image with 1 SD.

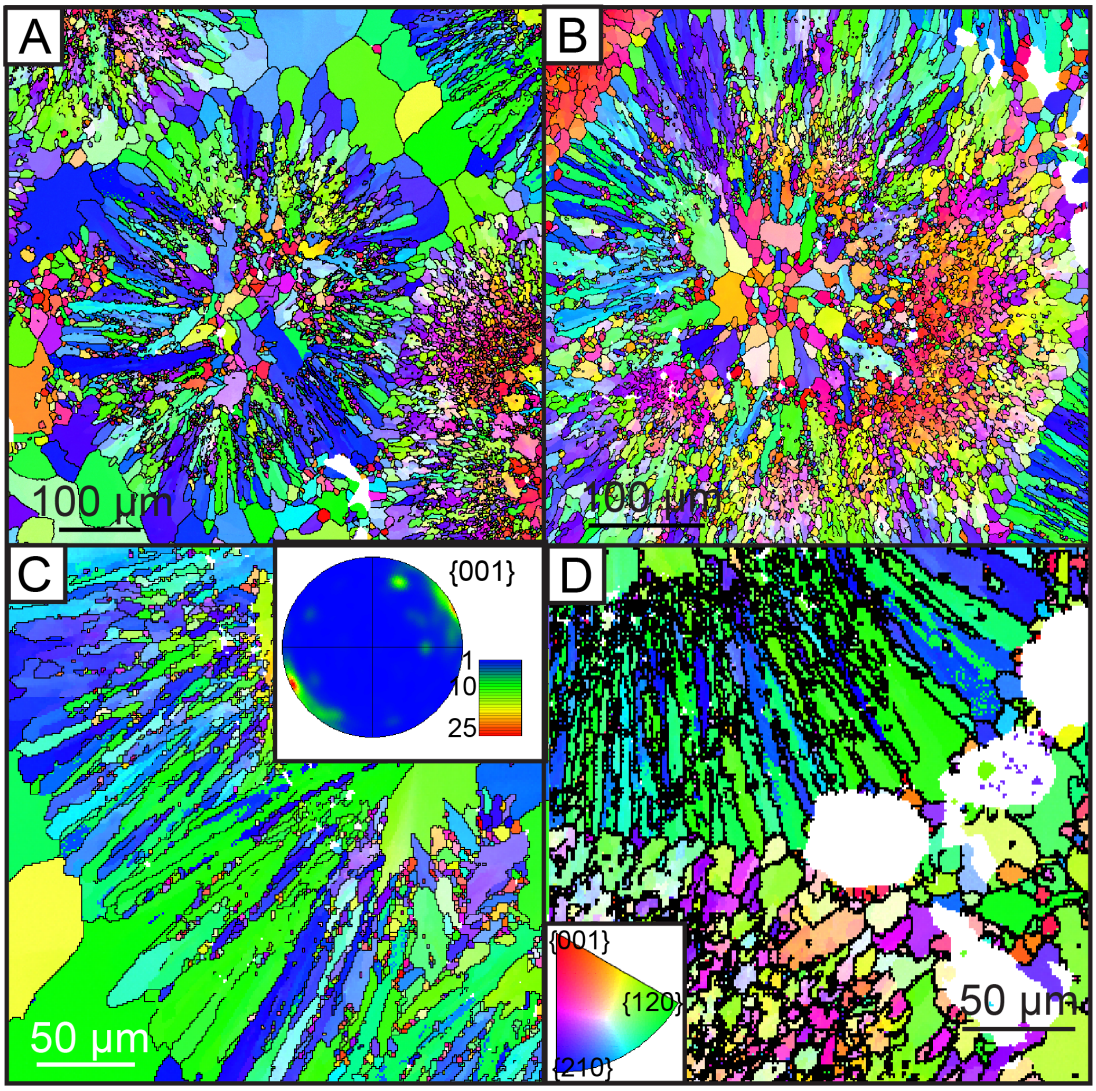

Fig. S5. Electron backscatter diffraction (EBSD) maps of ooid grain orientation plotted as inverse pole figures in the z-direction. (**a**) ooids cemented by calcite spar. Note the preservation of crystallographic orientations related to the radial ooid fabric. (**b, d**) ooids from a detrital-rich interval with a highlight of one side of an ooid (**c**) zoom in of upper right corner of a with a pole figure of grain orientation in the 001 direction.

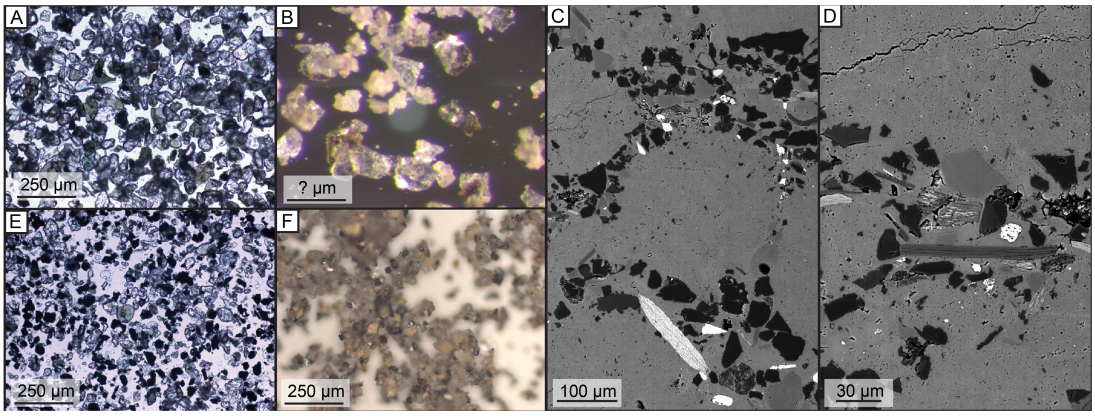

Fig. S6. Siliciclastic fraction of the Shuram (a–d) and Johnnie formations (e–f). (**a, e**) Wet grain mount under 10X magnification with visible biotite and muscovite grains. Iron oxides are more abundant in the sample from the Johnnie Formation. (**b, f**) Dry grain mount with quartz, muscovite, biotite, iron oxides and feldspars visible. The coarser grains from a fine-grained sandstone from the Shuram Formation include poorly weathered micas. (**c, d**) SEM images of iron-rich biotite grains within the detrital sediments filling in around the ooids.

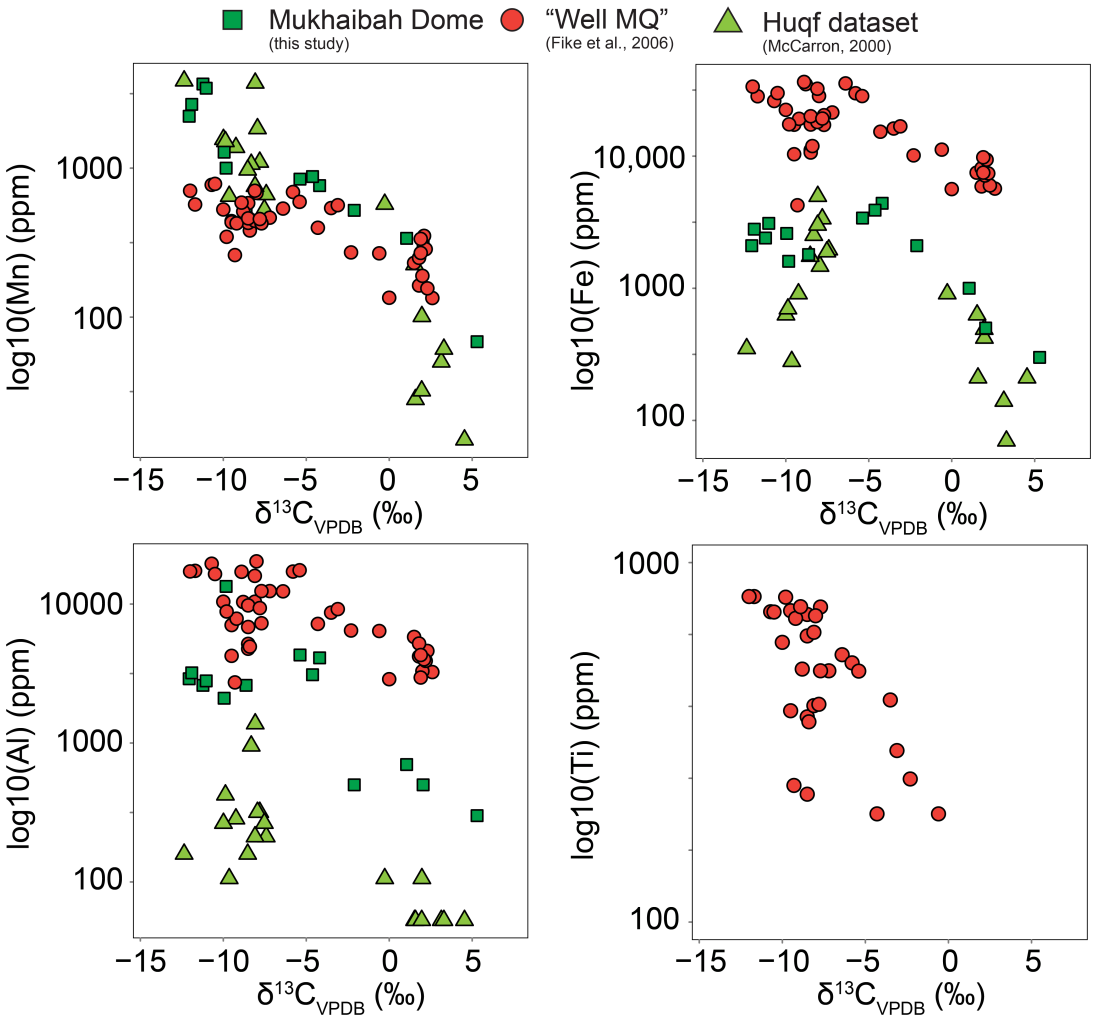

Fig. S7. Cross plots of bulk trace metal measurements versus δ^{13}C. a Log(Fe), log(Mn), log(Ti) and log(Al) versus δ^{13}C from three of the different sections analyzed. The magnitude of Fe, Al and Ti is higher for Well 'MQ' because that study dissolved well cuttings containing both siliciclastic and carbonate components in a strong acid as opposed to preferentially sampling carbonate. Data from this study and (*9, 101*).

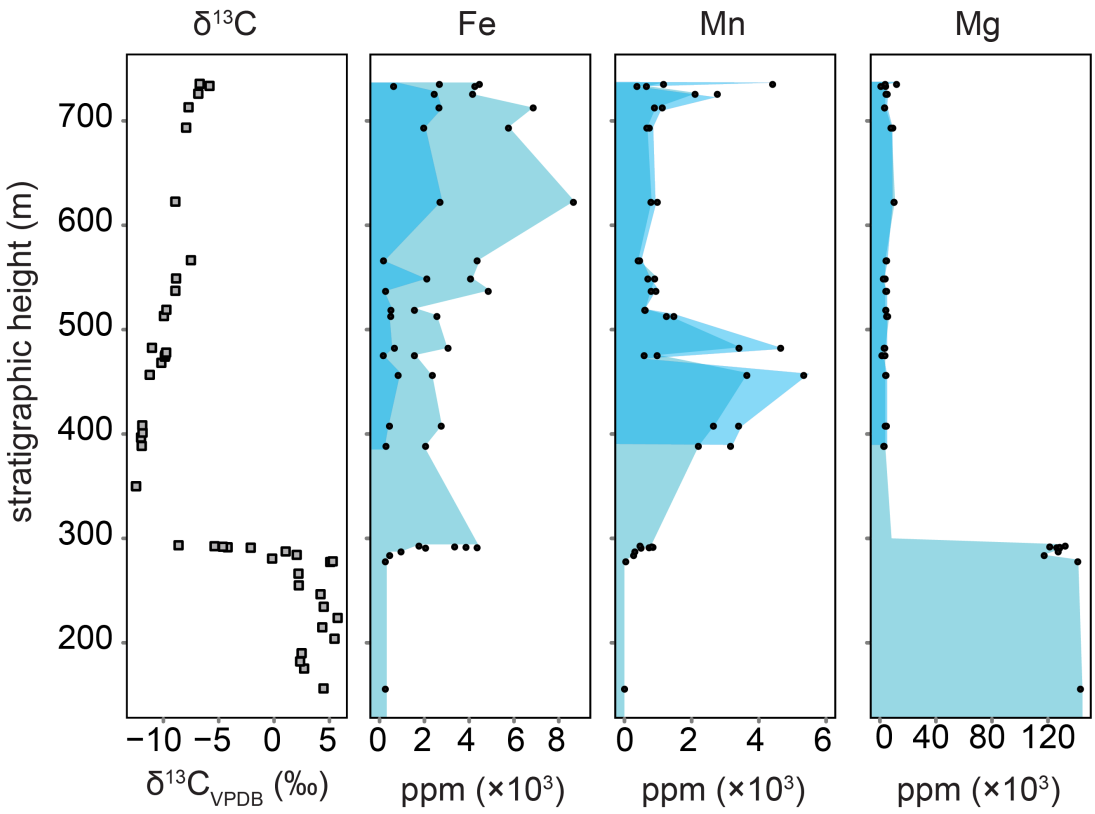

Fig. S8. Bulk strong acid (aqua regia) and acetic acid trace metal measurements from section MD for Fe, Mn and Mg. A strong acid dissolution (light blue) vs. an acetic acid dissolution (dark blue) targeting only the limestone indicates a significant component of the iron signal is not carried in the carbonate while most of the manganese signal is. The magnesium concentration confirms the observed mineralogical change to limestone.

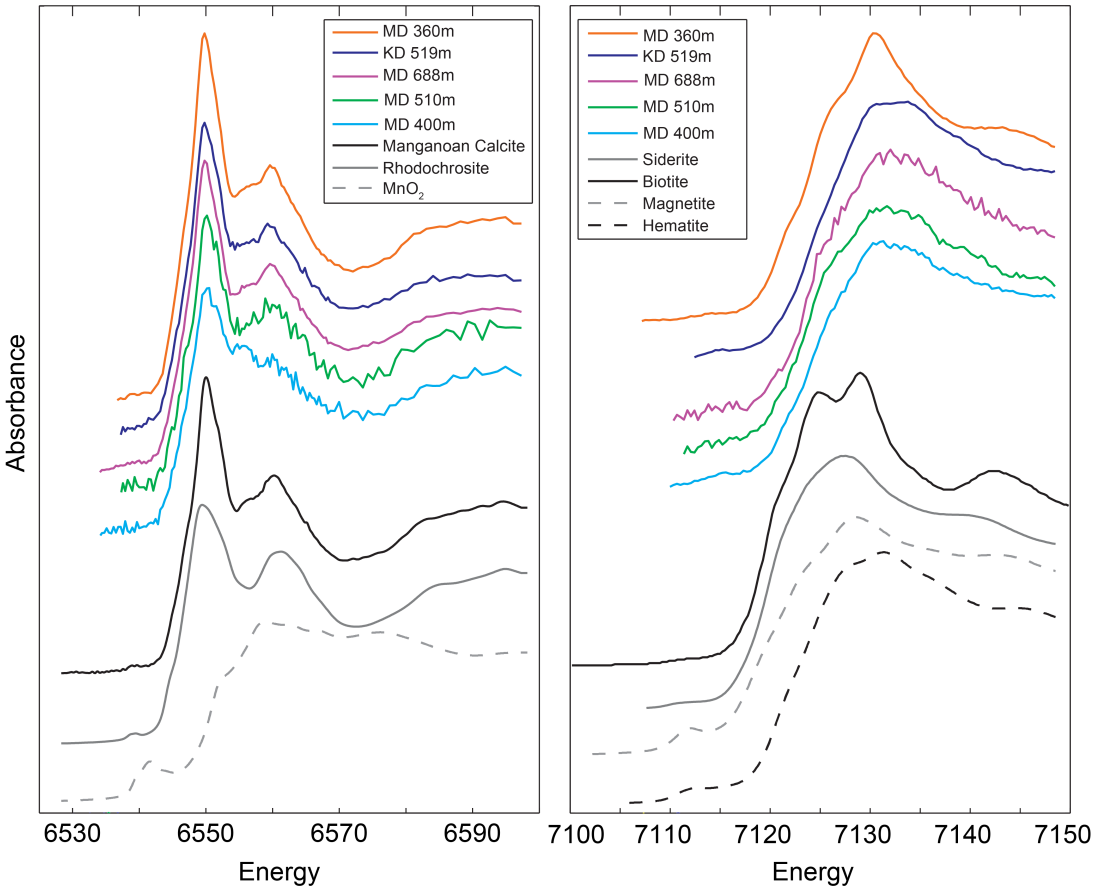

Fig. S9. Bulk XANES spectra of samples from the Shuram Formation. XANES spectra of samples from the nadir of the excursion yield consistent results indicating the iron is found in two phases hematite and biotite while the manganese is present as Mn(II) and most closely matches the spectra of manganoan calcite.

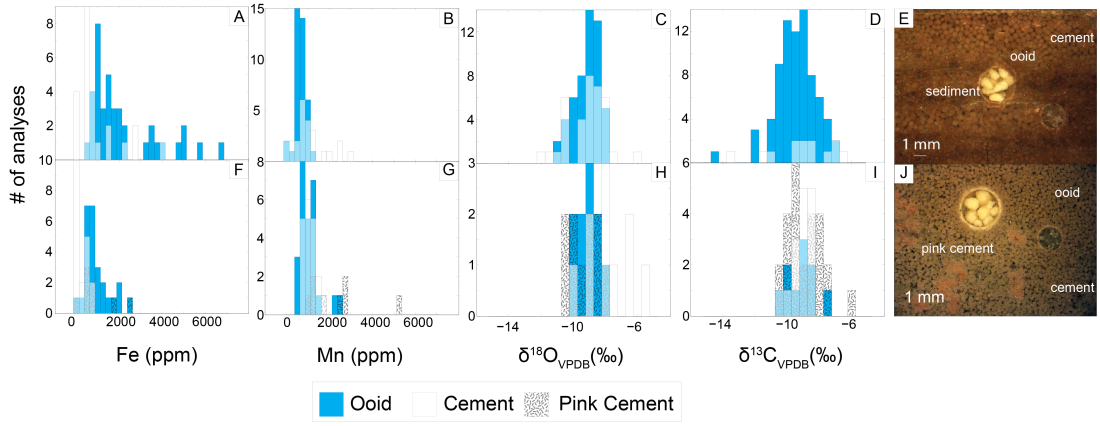

Fig. S10. Histograms of in situ geochemical data for two samples from the Shuram Formation. a, f Spot analyses of iron (ppm) on ooids and two cement types—clear blocky cements and pink microcrystalline cements. **b, g** Spot analyses of manganese (ppm). **c, h** Spot analyses of $\delta^{13}C_{VPDB}$. d, i, spot analyses of $\delta^{18}O_{VPDB}$. **e, j** Images of each sample showing ooids, two types of cements and embedded standards (± 1‰ SD).

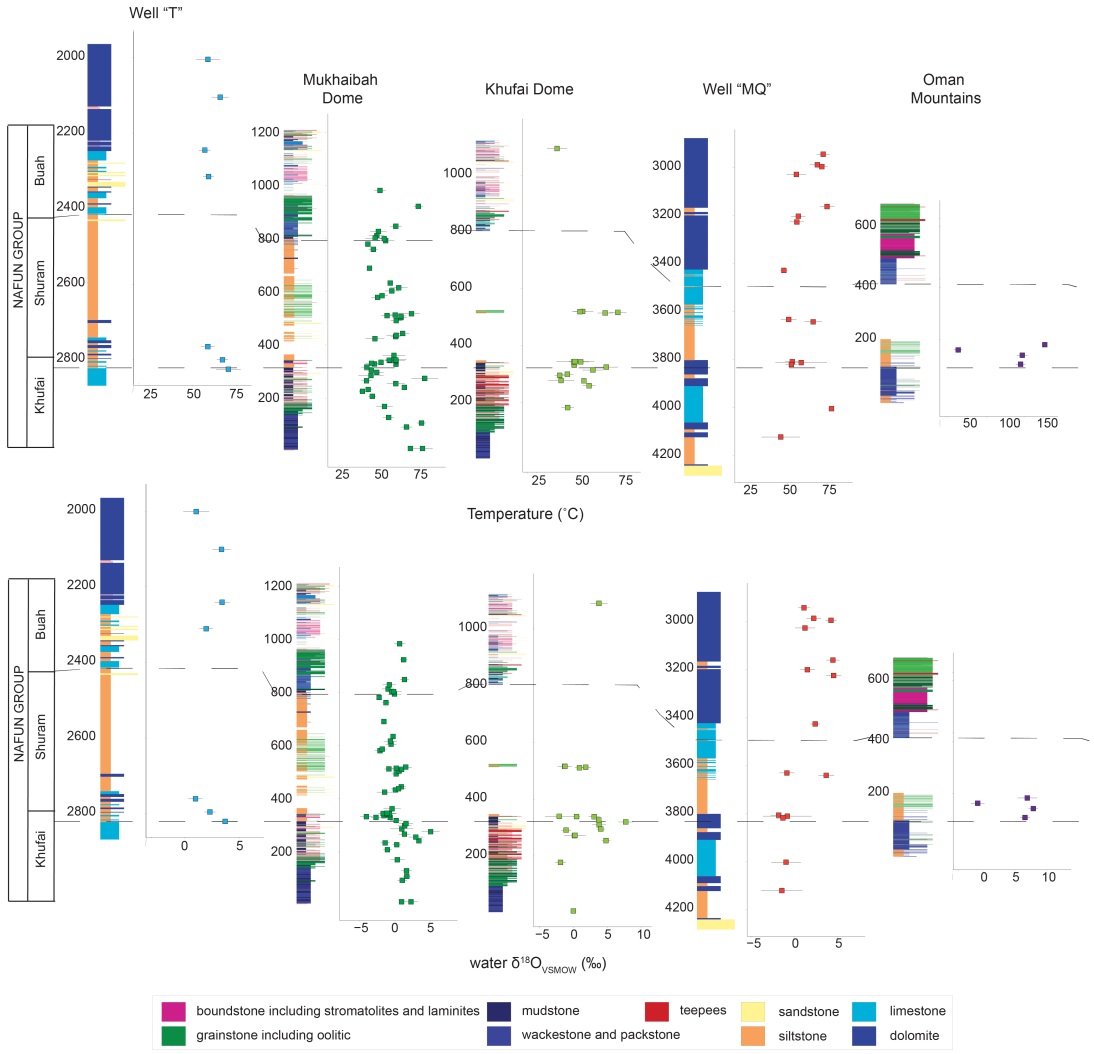

Fig. S11. Measured clumped isotope temperatures and estimates of water $\delta^{18}O_{VSMOW}$ values for samples from the five sections analyzed. Wells 'TM-6' and 'MQ-1' are plotted versus their current burial depth whereas 'MD' 'KD' and 'MTN' are plotted versus stratigraphic height. The sections are aligned on the onset of the Shuram excursion, which corresponds to a sequence boundary in the outcrop sections 'MD' and 'KD' outcrop stratigraphy from this study (Shuram and Buah fms.) and (Khufai Fm. (*39*))

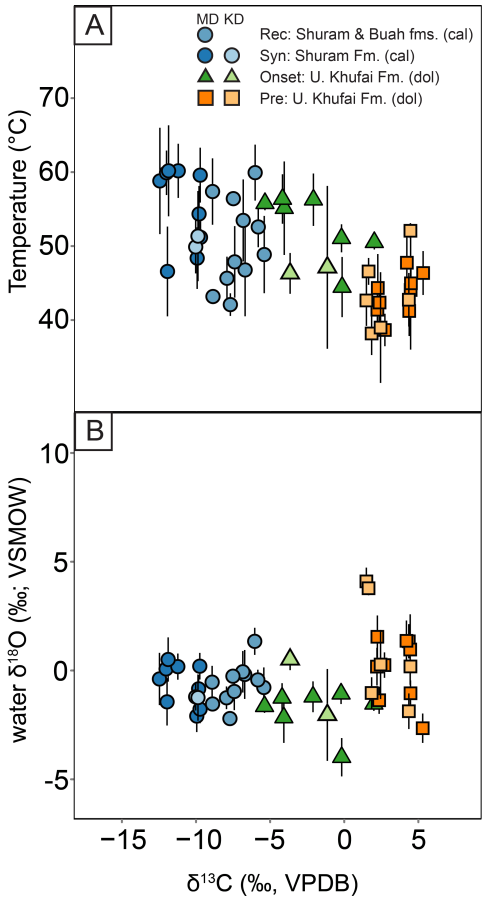

Fig. S12. Temperature and water oxygen isotopic composition vs. δ^{13}**C a** δ^{13}C vs. Temperature indicates on average lower temperatures in pre-excursion carbonates and equivalent temperatures between dolomites in the onset and limestones in the nadir of the excursion. **b** δ^{13}C vs. water $\delta^{18}O_{VSMOW}$ indicates a shift from elevated water $\delta^{18}O_{VSMOW}$ values in peritidal facies to open marine seawater-like oxygen isotope compositions. Circles are calcite.

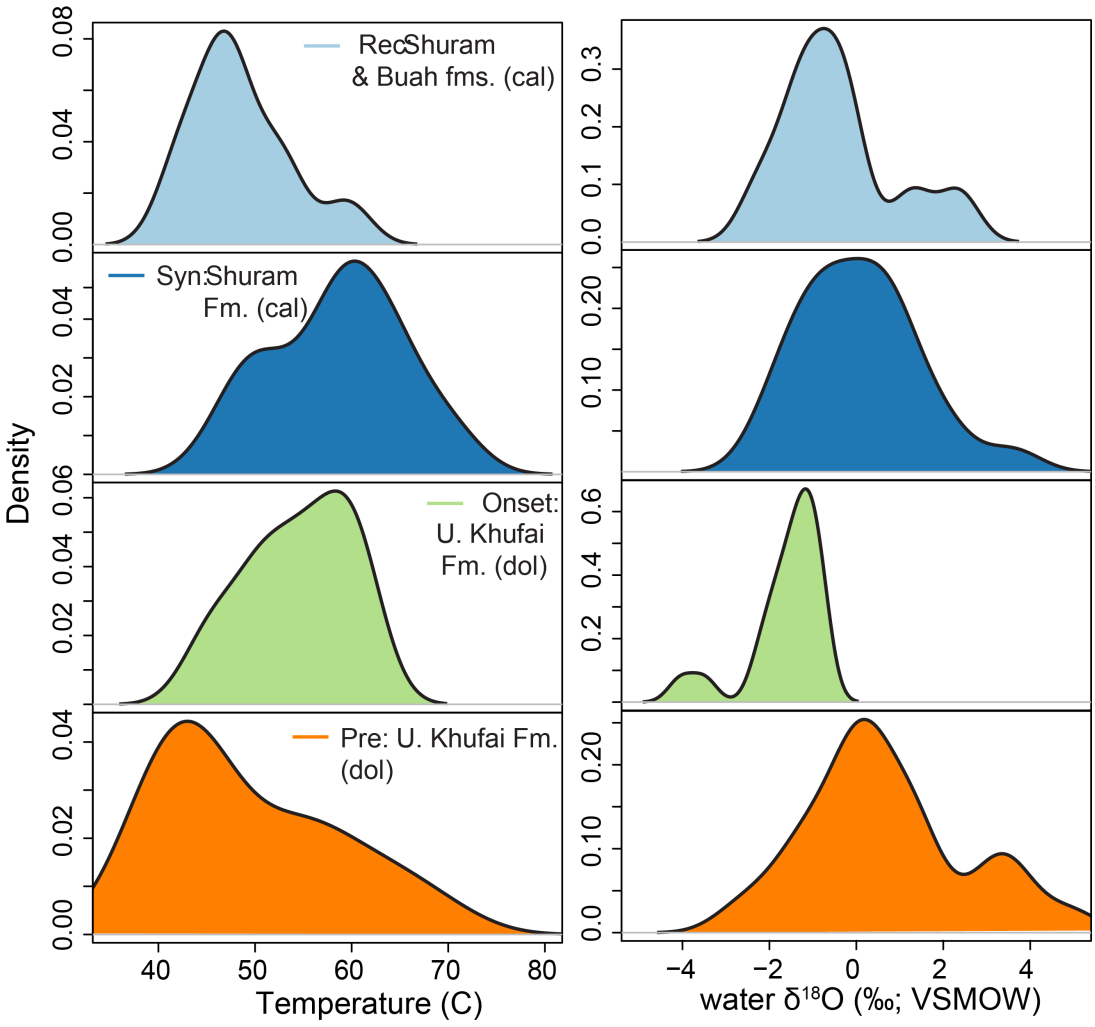

Fig. S13. Density distributions of the four populations (Pre-, Ons-, Syn-, Rec-) defining the excursion for temperature and water $\delta^{18}O_{VSMOW}$. Some populations are more skewed than other populations.

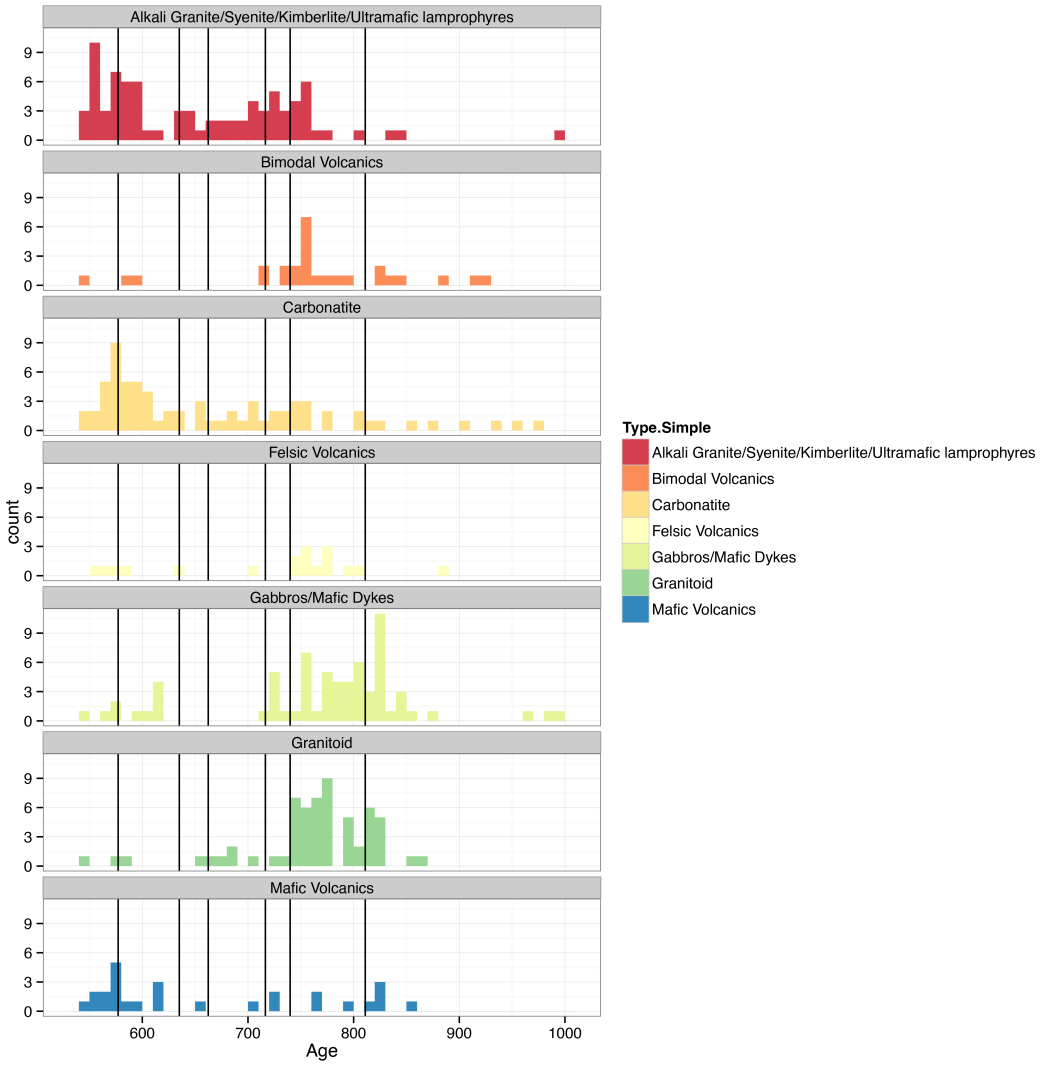

Fig. S14. Occurrence of Neoproterozoic igneous and volcanic rocks by type Each unit is counted once for its occurrence/appearance for each igneous rock type. Vertical lines are large negative carbon isotope perturbations.

Table. S1. Datasets from this manuscript Data from GPS, clumped isotope thermometry, XRD, bulk strong and weak acid trace metal analyses, SIMS, Electron microprobe and carbon and oxygen analyses.